

Master Thesis

**Lagrangian particle dispersion modeling of
stable carbon isotope ratios to track the
chemical aging of biomass burning aerosol**

Clara Betancourt
Institute for Geophysics and Meteorology
University of Cologne

1 April 2019

Supervisors

Prof. Dr. Susanne Crewell,
University of Cologne
Prof. Dr. Astrid Kiendler-Scharr,
Jülich Research Center

Contents

Acknowledgements	v
Abstract	vii
1. Introduction	1
1.1. Research objectives	2
1.2. Stable carbon isotope ratios	3
1.3. Lagrangian modeling	8
1.4. Set-up for this study	11
2. FLEXPART modeling	15
2.1. Model description	16
2.2. Folded retroplume technique	21
3. Sensitivity studies	25
3.1. Driving meteorological input data.	26
3.2. Chemical aging	28
3.3. Deposition	30
3.4. Folding receptor sensitivities to source regions with biomass burning emissions .	32
3.5. Summary	34
4. Case study	35
4.1. Ambient observations of levoglucosan concentration and isotope ratio	35
4.2. FLEXPART runs vs. ambient observations	36
5. Conclusion and future research	41
A. Fortran/IDL code	43
B. Tabular results	45
Bibliography	55

Acknowledgements

Many thanks to Dr. Iulia Gensch, for being a great mentor at Jülich Research Center. I am grateful for our fruitful discussions and the professional and personal advice.

I would also like to thank the supervisors of this thesis, Prof. Dr. Susanne Crewell from the University of Cologne and Prof. Dr. Astrid Kiendler-Scharr from the Jülich Research Center for their professional support and constructive feedback.

Futhermore, Dr. Dieter Gladtke and Dipl.-Ing. Uta Sager from the Landesumweltamt NRW provided information on the used aerosol samples, and were cooperative and helpful contact persons. Prof. Dr. Jochen Rudolph from the Jülich Research Center shared his extensive knowledge about isotope research. Sabine Schröder from the Jülich Supercomputing Center and Dr. Ignacio Pisso from the Norsk Institutt for Luftforskning helped to set up the new wet deposition module of FLEXPART. Dr. Olaf Stein from the Jülich Reseach Center provided meteorological input data for the model runs.

Thanks a lot to Beatrix Kammer, Dr. Tammarat Piansawan, Christoph Küppers and Christin Waldorf from the Stable Isotopes Group in Jülich for performing the complex isotopic measurements that are the experimental basis of this thesis. I appreciated very much the blend of laboratory work and modeling.

Last but not least, thanks to my family and friends for patience, encouragement and support.

Abstract

Biomass burning is an important source of atmospheric pollutants in gas and particulate phase. These have an impact on air quality, health and climate. Domestic heating with firewood is a major source of fine dust in Germany in the cold season. So there is a strong scientific interest to accurately quantify the contribution of local to remote sources to the aerosol burden.

In this work, a modeling methodology is developed to simulate concentration and isotope ratios of the biomass burning tracer levoglucosan. To this end, retroplumes obtained with the Lagrangian Particle Dispersion Model (LPDM) FLEXPART are folded with country-specific emission inventories. Since isotopes can provide additional information on source and processing of the sampled aerosol, the option to output stable carbon isotope ratios of levoglucosan is implemented in the model. Sensitivity studies are conducted to determine governing processes in the employed model. Furthermore, the established modeling routines are applied in a case study, with the goal to assess the contribution of local vs. remote emissions from firewood domestic heating to the particulate matter sampled at two measurement stations of the North Rhine-Westphalia Landesumweltamt (LANUV). This study focuses on 50 selected aerosol samples taken at an urban background station in Mülheim-Styrum and at a rural background station in the Eifel, in the cold seasons of 2015-2017. The measured concentration and isotopic composition of the sampled levoglucosan are used to validate the modeling method.

The results show a good agreement between modeled and observed concentrations. It is though shown that at the urban station, concentration measurements are partly influenced by unresolved sources near by the sampling station. According to the model outcome, the largest part of the sampled aerosol is 1-2 days old, and thus originates from local to regional sources. Consequently, chemical aging has a minor influence on the levoglucosan concentration and isotopic composition in the modeled period. Additionally to the short atmospheric residence time, a low OH-concentration in the cold season hinders chemical decay. On that account, it can be concluded that the observed δ -value variances are caused only by variances in the isotope ratios at sources. The sensitivity studies indicate that the main sink for the investigated biomass burning aerosol is wet deposition. For aged aerosol in the coarse mode, also gravitational settling is a considerable loss process.

This work shows that combining Lagrangian modeling with isotopic- and concentration measurements, reliable information on the biomass burning aerosol source is provided. The findings show that the biomass burning aerosol burden in living areas is of local origin and thus it can be mitigated by reducing local emissions. Yet, a comprehensive benchmarking of source specific isotopic ratios is still missing. Furthermore, modeling studies investigating large scale fires in summer are required, since they have the potential to contribute to aging understanding.

1. Introduction

Organic aerosol (OA) has anthropogenic and biogenic sources, being either released as primary OA (POA), or formed as secondary organic aerosol (SOA) from volatile organic compounds (VOC). Most of the anthropogenic emissions originate from fuel combustion and biomass burning. The biogenic particles are predominately SOA formed by the oxidation of biogenic VOC. In the atmosphere, OA undergoes various transport, aging and deposition processes, such as photolysis and photo oxidation, sedimentation or wash-out. Particles have a direct radiative effect by absorbing and scattering solar radiation. Moreover, they act as cloud condensation nuclei (CCN), leading to cloud formation which indirectly impacts the radiation budget. Being exposed to OA, humans experience severe health impairments such as cardiovascular and respiratory diseases. Thus OA affects air quality, health and climate.

Biomass burning is an important source of OA. Biomass burning includes natural and man-made fires such as forest fires, agricultural fires and domestic heating/cooking fires. Hallquist et al. [2009] estimated that biomass burning releases 42 Tg C/a into the atmosphere, which is about a quarter of the global emitted particulate carbon. Such estimates are associated with considerable uncertainties. Parts of the uncertainties result from the little known source distribution and strength, but also from a lack of understanding the mentioned degradation and deposition processes. Since biomass burning contributes substantially to the OA hazards, it is of great scientific and societal interest to accurately apportion sources and thus improve the estimates of the biomass burning aerosol burden at local to global scales.

In Germany, small wood stoves in the residential sector provide only 1.5 % of the total energy supply, but contribute 16 % to the total PM_{2.5} emissions. This is comparable to the total road traffic exhaust of PM_{2.5} (Amann et al. [2018]). Successful policy interventions for effective air pollution mitigation require integrated approaches. Here, an accurate apportionment of local emissions versus regional transport is necessary.

For the source apportionment of biomass burning aerosol, factor analysis, chemical mass balance and Lagrangian techniques are employed (e.g. Zheng et al. [2002], D. Busby et al. [2015]). For chemical mass balance modeling, the source specific molecular tracer levoglucosan was used (e.g. Fine et al. [2002]). Levoglucosan is the ideal tracer for biomass burning, because it is only formed by the thermal breakdown of cellulose, and it is emitted in large quantities during biomass burning. It was employed as a non-reactive marker in the above-mentioned studies. The accuracy of these studies is limited by considerable uncertainties in the emission factors, and by the fact that levoglucosan was recently proven to be chemically unstable (Hennigan et al. [2010], Sang et al. [2016]). Recent laboratory studies have shown that levoglucosan reacts with OH radicals within a lifetime of ca. seven days under typical atmospheric conditions

1. Introduction

(Sang et al. [2016]). This new finding opens up new potential applications, especially in the field of isotopic analyses.

Sources of biomass burning aerosol can be significantly better constrained by taking into account the stable carbon isotope ratio of levoglucosan. This option is based on two properties of isotopes: OA emissions have a certain source isotopic composition, the 'isotopic fingerprint'. Furthermore, chemical processing leads to isotopic fractionation due to the kinetic isotope effect (KIE), which is specific for each reaction ('isotopic footprint'). Consequently, highly innovative source apportionment methods aim to combine trajectory and wind-based models with isotopic analyses, which deliver additional information for validation. Recently, Gensch et al. [2018] used isotopic measurements together with the Lagrangian particle dispersion model FLEXPART (Stohl et al. [2010]) to investigate chemical aging processes in biomass burning aerosol. To this end, the photochemical age of particulate levoglucosan was derived firstly from isotopic ratios and secondly from back trajectory simulations. Here, a post-modeling numerical approach was developed to quantify the impact of mixing with freshly emitted levoglucosan on the isotopic composition. The results of these two independent methods agreed well on average. This shows that the degree of photo oxidative aging of particulate levoglucosan can be quantified by combining laboratory KIE studies, observed isotopic composition at sources and in the field, as well as back trajectory analyses. Yet the scatter in the individual data pairs pointed out the need to improve the identification and distinction of contributions from different source types to the sampled levoglucosan, which is possible by using the full dispersed output of FLEXPART.

1.1. Research objectives

The main research objective of this work is to develop an improved modeling framework for the source apportionment of biomass burning aerosol and its atmospheric processing. FLEXPART will be employed to obtain a comprehensive description of the aerosol transport and turbulent diffusion. Compared to Gensch et al. [2018], individual sources of investigated aerosols will be constrained in more detail by using the full dispersed output of the model. Loss processes (chemistry and deposition) will be treated during the runs, not in the post-processing calculations. Isotopic- and concentration measurements in ambient biomass burning aerosol samples will be used to validate the model.

The main tasks are

1. to introduce ^{13}C -levoglucosan as an additional model tracer. It has the same properties as the isotopologue containing only ^{12}C , except for a slightly different rate constant for the reaction with the OH radical due to the KIE. The full dispersed modeling output of the backward simulations give the emission sensitivity for ^{12}C - and the ^{13}C -levoglucosan, making possible post processing isotopic ratio calculations at the receptor.
2. to carry out sensitivity studies by varying critical input and model parameters. These sensitivity studies show which sources and processes can be distinguished best. Moreover, they provide uncertainty estimations.
3. to assess by a closure study the contribution of local residential heating to the biomass burning aerosol burden in the cold season in North Rhine Westphalia, Germany. For aerosol samples collected at two LANUV (NRW Laender Environmental Agency) sites during winter/heating time, levoglucosan concentration and isotope ratio are measured. The observations are compared to modeling results to determine the local and regional quality of air vs. that of masses transported over long distances and across national borders.

In this Chapter, terms and principles of using stable isotope analyses in atmospheric research are introduced. The theoretical part (Chapter 2) provides a model description of the Lagrangian particle dispersion model (LPDM) FLEXPART, and a formal derivation of the necessary steps to calculate concentration and isotopic composition at the receptor. Sensitivity studies are presented in Chapter 3. The newly developed modeling techniques and configuration are applied in the case study shown in Chapter 4. The findings from Chapter 2-4 and their significance are discussed in Chapter 5. Here, the achievements are assessed as a whole, including overall uncertainties as well as the applicability of the developed techniques for future studies.

1.2. Stable carbon isotope ratios

Stable carbon isotope ratios of levoglucosan are applied in atmospheric studies to provide additional information on the source and processing of biomass burning aerosol. Figure 1.1 depicts the formation and fate of biomass burning aerosol, including the isotopic fractionation of levoglucosan through chemical aging. Levoglucosan is formed during biomass burning by the thermal break-down of cellulose. The emission has a source specific isotopic ratio (‘isotopic fingerprint’). During transport through the atmosphere, levoglucosan is photo oxidized by hydroxy radicals (OH). Its initial isotopic ratio then changes due to the reaction specific KIE (‘isotopic footprint’). These properties are described by the ‘isotopic hydrocarbon clock’-equation (Equation 1.4). The underlying theory is elaborated in this Section.

1. Introduction

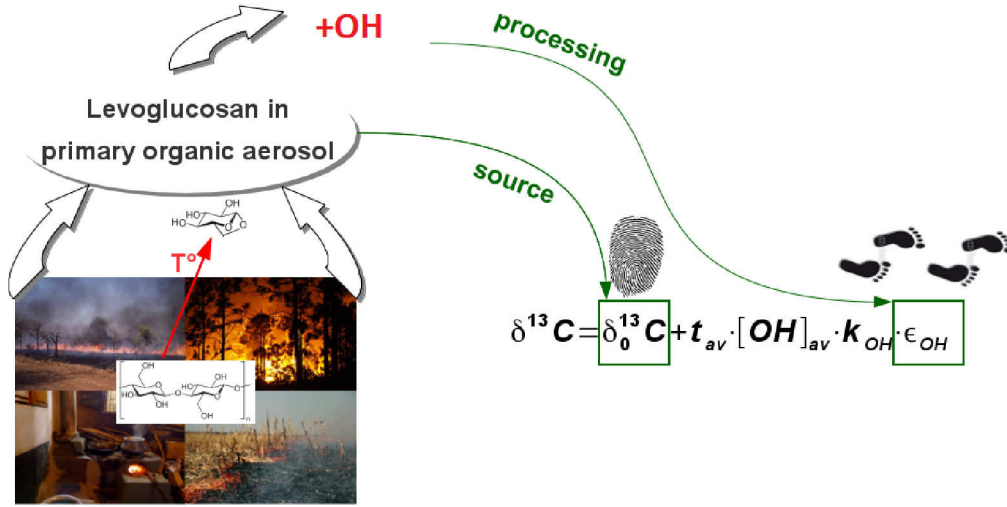


Figure 1.1.: Change of levoglucosan isotopic composition due to chemical aging, described by the ‘isotopic hydrocarbon clock’-equation. The isotopic composition $\delta^{13}\text{C}$ of a sample depends on its isotopic composition at the source $\delta_0^{13}\text{C}$, its photochemical age $t_{av} \cdot [\text{OH}]_{av}$, the reaction constant k_{oh} and the KIE, expressed as ϵ_{OH} .

Isotopic ratio measurements. Carbon has two naturally occurring stable isotopes ^{12}C and ^{13}C , which account for ca. 99 % and 1 % of the total carbon respectively. Due to the difference in the nuclear masses, physical and chemical processing in the atmosphere results in an inhomogeneous ambient isotope distribution. The stable carbon isotope ratio $R = ^{13}\text{C}/^{12}\text{C}$ is expressed as a δ -value.

$$\delta^{13}\text{C} = \frac{(^{13}\text{C}/^{12}\text{C})_{\text{sample}} - (^{13}\text{C}/^{12}\text{C})_{\text{ref}}}{(^{13}\text{C}/^{12}\text{C})_{\text{ref}}} \times 1000 \text{ ‰} \quad (1.1)$$

The ratio $(^{13}\text{C}/^{12}\text{C})_{\text{sample}}$ is compared to that of a reference substance¹ $(^{13}\text{C}/^{12}\text{C})_{\text{ref}}$, to ensure intercomparability between different measurements. Since variations in the isotopic composition are usually small, the δ -value is expressed in per mil.

Isotopic measurements of levoglucosan in ambient aerosol filter samples are challenging and costly. The compound of interest is mixed with other pollutants on the filter material. Ambient levoglucosan concentrations are usually in the ppt-range, which results in small sample sizes. In addition, atmospheric variations in $\delta^{13}\text{C}$ are in the per mil-range, which is challenging for the precision of measurements. Levoglucosan isotopic ratio measurements are done via two dimensional gas chromatography, coupled on line to isotope ratio mass spectroscopy (2D-GC–

¹Vienna Pee Dee Belemnite (VPDB) with $^{13}\text{C}/^{12}\text{C}_{\text{VPDB}} = 0.0112372$ (Craig [1957])

1.2. Stable carbon isotope ratios

IRMS, described e.g. by Gensch et al. [2018]). This method is compound specific. Due to the effective two-column chromatographic separation, it is suitable to be applied to measure isotopic ratios of the highly polar compound levoglucosan. It is precise in the sub-‰-range even for small sample sizes down to 10 ng (Gensch et al. [2018]).

The isotopic composition of levoglucosan at sources is influenced by that of the parent material, being independent of the combustion conditions. Sang et al. [2012] determined levoglucosan $\delta^{13}\text{C}$ in aerosol from the combustion of selected C3 plants. Wood smoke of combusted samples was collected on filter material and isotopically analyzed. The served δ -values were in a range of -25.6 to -22.2‰, showing an enrichment in ^{13}C of 2‰ for the softwood samples (coniferous trees), compared to the rest of burned plants.

Kinetic isotope effect. In the atmosphere, levoglucosan is photo oxidized by OH-radicals. The reaction influences the isotopic composition of levoglucosan, because molecules containing a heavier stable carbon isotope are oxidized at a different rate than the molecules containing only ^{12}C . This effect, caused by the weak mass dependence of the reaction rate constant, is termed kinetic isotope effect (KIE). Since KIE is reaction specific, it can be considered as an 'isotopic footprint' of the atmospheric degradation. KIE is defined as the rate constant ratio of the levoglucosan molecules containing only ^{12}C atoms and the molecules containing a ^{13}C atom.

$$KIE = \frac{{}^{12}k}{{}^{13}k} \quad (1.2)$$

The difference in reactivity is usually small, so KIE is expressed as an ϵ -value in per mil.

$$\epsilon = (KIE - 1) \times 1000 \text{‰} \quad (1.3)$$

Molecules containing a heavier isotope usually react slower, inducing the so called *normal* KIE. The faster processing of light isotopes leads to an enrichment of ^{13}C in the reactant with time.

KIEs are determined in reaction chamber studies. The examined compound is exposed to the oxidizing agent. The concentration and the isotopic fractionation of the reactant are monitored over time. Sang et al. [2016] determined the KIE of the levoglucosan oxidation by OH radicals. Levoglucosan in both particles and aqueous solution was exposed to gaseous OH, showing ϵ_{OH} -values of $2.29 \pm 0.18 \text{‰}$ and $1.87 \pm 0.18 \text{‰}$ respectively.

Photochemical age. For the source apportionment of atmospheric biomass burning aerosol, as well as the extent of processing, it is essential to determine the photochemical age of the pollutants, describing their time integrated exposure to OH radicals. Stable carbon isotope ratios of levoglucosan can be used to determine the photochemical age of biomass burning

1. Introduction

aerosol. This principle is deduced from the 'hydrocarbon clock' concept. According to that, the photochemical age of a sample can be derived by considering the concentration ratio decay of two co-emitted tracers from the respective source. Here, both lifetimes and emitted concentrations of the tracer pair have to be known and comparable. It is often problematic to find such a pair.

Combining the levoglucosan isotopes ^{12}LG and ^{13}LG ideally fulfills the above mentioned requirements due to similar lifetimes and emitted concentrations. Due to small KIEs, the photochemical age of a single compound can be linearly weighted. Instead of an exponential expression, the linear 'isotopic hydrocarbon clock' can be applied (Rudolph and Czuba [2000]).

$$\delta^{13}\text{C}(t) = \delta_0^{13}\text{C} + t_{av} \cdot [\text{OH}]_{av} \cdot k_{OH} \cdot \epsilon_{OH}, \quad (1.4)$$

In this Equation, $\delta^{13}\text{C}(t)$ represents the δ -value at the sampling point, $\delta_0^{13}\text{C}$ the initial δ -value at the emission source, $t_{av} \cdot [\text{OH}]_{av}$ the average photochemical age of the sample and $[\text{OH}]_{av}$ the average OH concentration the tracer was exposed to. The advantage of applying the 'isotopic hydrocarbon clock' is that the photochemical age of a **single** species can be determined by its isotopic ratio when knowing the δ -value at the source and the KIE of its atmospheric degradation. By averaging, an evaluation of the measured isotope ratios is possible, even if the sample consists of mixed contributions with different photochemical age. Moreover, unbiased $[\text{OH}]_{av}$ can be derived, when the Equation 1.4 is combined with an independent approach to estimate t_{av} , e.g. with transport modelling Gensch et al. [2018].

Two-endpoint mixing. If considering only mixing and no chemical processing, the isotopic composition of air pollutants results from mixing of air masses with different concentrations and different δ -values. A source can often be regarded as a plume with a high concentration that is emitted to the atmosphere with a constant background concentration. This concept is termed two-endpoint mixing. The resulting atmospheric δ -value thus depends on the respective concentrations c [$\mu\text{g}/\text{m}^3$], volume fractions f [m^3/m^3] and δ -values:

$$\delta_{atm} = \frac{\delta_{emis} \cdot c_{emis} \cdot f_{emis}}{c_{atm}} + \frac{\delta_{backgr} \cdot c_{backgr} \cdot f_{backgr}}{c_{atm}} \quad (1.5)$$

If a small volume of high concentration mixes with large volume of low concentration, the resulting δ_{atm} -value simplifies to (Rudolph [2007])

$$\delta_{atm} = \delta_{emis} + \frac{\Delta\delta \cdot c_{backgr}}{c_{atm}}, \quad (1.6)$$

where $\Delta\delta$ denotes the difference $\delta_{backgr} - \delta_{emis}$. So called 'Keeling plots' contain δ_{atm} , plotted against $\frac{1}{c_{atm}}$. Equation 1.6 shows that the y-intercept of a Keeling plot is the δ -value of the

1.2. Stable carbon isotope ratios

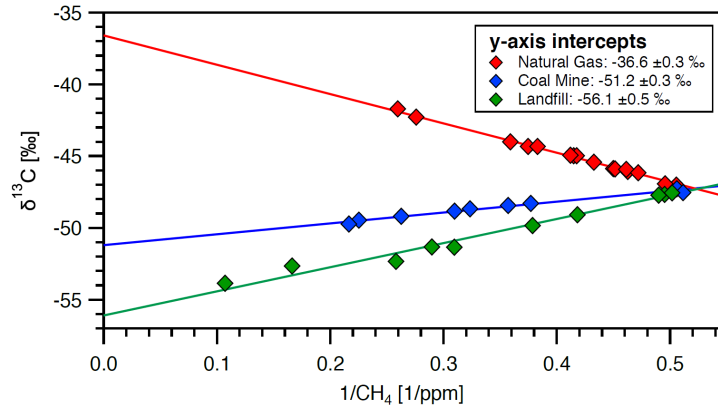


Figure 1.2.: Keeling plot of the inverse mass mixing ratio of methane vs. its stable carbon isotope ratio for measurements at different industrial sites in the United Kingdom (Zazzeri et al. [2015]).

emission (δ_{emis}). The slope ($\Delta\delta \cdot c_{backgr}$) describes the influence of background aerosol to the atmospheric δ -value. From the product $\Delta\delta \cdot c_{backgr}$, neither $\Delta\delta$ nor c_{backgr} can be resolved individually. An independent approach like describing the background by global modelling is required.

To illustrate this principle, Figure 1.2 shows δ_{atm} of methane samples from different sites in the United Kingdom, plotted as a function of $1/c_{atm}$. The concept of two-endpoint mixing is also applicable for the concentration and isotopic composition of levoglucosan from a biomass burning aerosol source and background.

Ambient studies. The concepts presented in this Section were developed based on isolated air parcels. As there are no such in reality, the challenge when interpreting isotope ratios in ambient studies is to combine mixing, degradation and loss processes. It is often difficult to track single processes because measurements are usually sparse ($n < 100$), and because prevailing emissions and meteorological conditions have to be well-known. The usual approach is a careful examination of the sampling situation, possible sources and complementary numerical atmospheric transport modeling.

A study on ambient isotopic measurements of levoglucosan in biomass burning aerosol was carried out by Gensch et al. [2018]. $\delta^{13}C$ was used to determine the photo chemical age of levoglucosan in aged ambient aerosol, based on the 'isotopic hydrocarbon clock'. Independently, the t_{av} was determined using backwards analyses from FLEXPART Lagrangian particle dispersion modeling. A post processing approach was developed based on the mixing layer height and the height of the centroid back-trajectories to describe the 'two-endpoint mixing' of fresh emissions with the aged levoglucosan. The overall good agreement between the simulated

1. Introduction

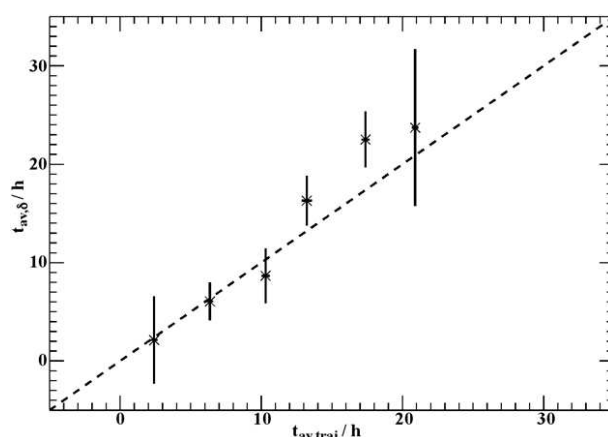


Figure 1.3.: Comparison of photochemical age determined by postprocessing centroid trajectory output of FLEXPART and by isotopic measurements in biomass burning aerosol sampled at Guangdong province, China, 2009 (Gensch et al. [2018].)

and observed photo chemical ages validated the developed approach (Figure 1.3). A practical finding of this study was that chemical loss of levoglucosan exceeded 50 % in one fifth of the analyzed samples. Thus the use of levoglucosan as a stable molecular marker likely underestimates the contribution of biomass burning to the aerosol burden. Nevertheless, the authors caution that the scatter of the individual data might be due to the simplifying assumptions, necessary in such a basic approach. The FLEXPART dispersed output represents an improvement of the simulations. They contain source-receptor sensitivity fields which might better constrain emission sources. Moreover chemical decay, dry and wet deposition are treated within the runs.

1.3. Lagrangian modeling

Atmospheric transport modeling, combined with measurements of stable carbon isotope ratios of levoglucosan in biomass burning aerosol, can provide a powerful tool to constrain pollution sources and atmospheric processing. Here, transport modeling gives a spatial additionally to the temporal dimension for the mixing and aging regimes. Furthermore measurements are used to validate a modeling method.

Lagrangian view. The two main types of atmospheric transport models are Eulerian models and Lagrangian models. Eulerian models divide the model domain in fixed grid boxes and regard the flow into and out of these boxes (Figure 1.4 a). Lagrangian models assess atmospheric properties by using a moving frame of reference to follow a model 'air parcel' (Figure 1.4 b). This point of view is advantageous when the fate of emissions is accessed, because individual

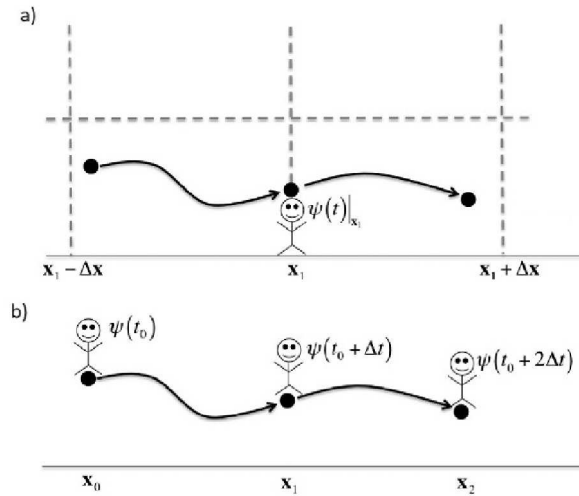


Figure 1.4.: Different concepts of atmospheric transport modeling. a) Lagrangian modeling: Atmospheric properties, described as a state variable Ψ are observed from a moving frame of reference. b) Eulerian modeling: Ψ is observed from fixed grid boxes (adapted from Lin [2013]).

air parcels can be tracked. There is no numerical diffusion, and errors are comparatively small because the model runs independently of a numerical grid. Thus Lagrangian modeling is especially convenient when the sampling/release sites have a small spatial extension and if small scale dispersion is of interest.

Lagrangian air parcels. Moving air parcels in Lagrangian models can be described in different ways (Figure 1.5). In mean trajectory models, the air parcel position is only affected by the mean wind, neglecting turbulence and dispersion. This approach is prone to significant error in turbulent regimes like the planetary boundary layer. In box models, the air parcel is represented by a cuboid whose size changes with the contained tracer mass. Gaussian puffs assume a three dimensional, growing plume with a Gaussian tracer distribution. However, these models naturally fail to describe the plume deformation by diffusion, turbulence or shear winds in detail. On the contrary, air parcels in LPDMs are represented by a stochastic amount of identical model ‚particles‘. These ‚particles‘ are infinitesimal air parcels that carry a fraction of the tracer mass. Dispersion is implemented by an individual random Markov process for each particle. Since the particles are independent of each other, the evolving shape of the air parcel is described precisely by the ensemble of particles. This approach simulates the effects of turbulence and dispersion best, but is computationally most expensive due to the large number of particles required.

1. Introduction

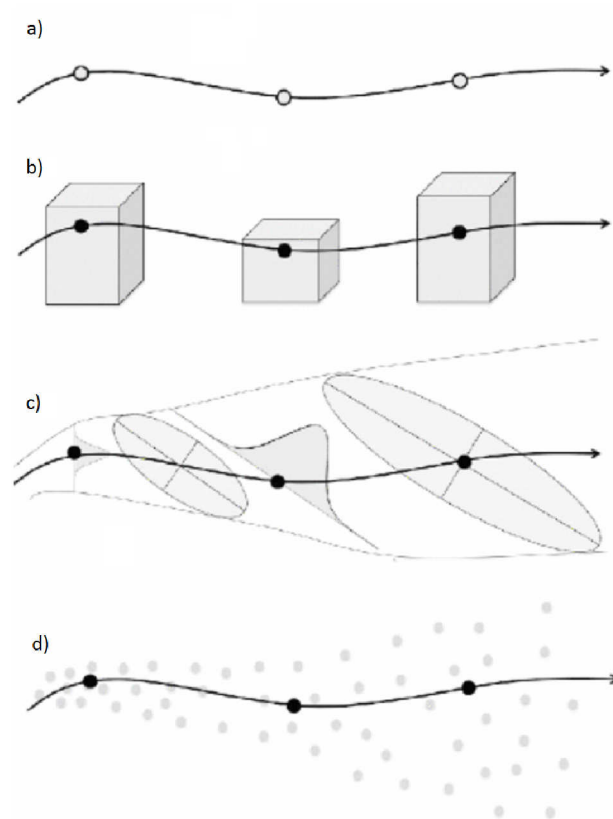


Figure 1.5.: Different representations of an air parcels in Lagrangian models: a) mean trajectories, b) box models, c) Gaussian puffs, d) particle plumes. Grey dots and shapes represent air parcels, black dots represent the center of mass (Lin [2013]).

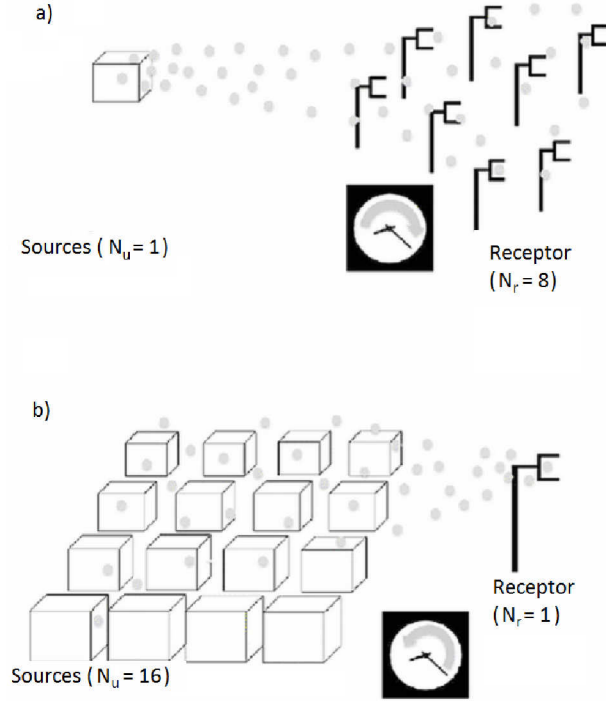


Figure 1.6.: Comparison of forward and backwards modeling. a): Forward modeling. One ($N_s=1$) source, depicted as a box, emits a tracer, which is then sampled at many receptor points ($N_r=8$). b): Backwards run. Many sources ($N_s=16$) emit the tracer, which is sampled at one location ($N_r=8$). Sources that do not contribute to the receptor are not considered. From Lin [2013]

Backwards modeling. If only first order processes are considered, a LPDM can be run backwards by reverting the time step of the advection of particles. The output of a backward run is a ,retroplume‘which resolves the influence of individual sources to the receptor.

The backwards mode is computationally advantageous if there are more potential sources than receptors, because only sources that contribute to the receptor are considered (Figure 1.6). The retroplumes can be combined with emissions using the ,folded retroplume technique‘. FLEXPART, the LPDM used in this study and the folded retromplume technique are described in detail in the theoretical part (Chapter 2).

1.4. Set-up for this study

According to the objectives of this study (Section 1.1), the modeling setup provides a framework for the source apportionment of biomass burning aerosol and its fate during transport. It is applied in sensitivity studies (Chapter 3) and the case study (Chapter 4).

1. Introduction

The methodology is depicted in Figure 1.7: Gridded meteorological input data delivers the necessary wind fields to describe transport by advection and diffusion. FLEXPART is run backwards from the sampling points to investigate the origin of the sampled air masses. Chemical loss and wet deposition are included in the run. The output of a backwards run is called 'retroplume', and represents sensitivity fields of the receptor to potential upwind sources. Retroplumes can be linked with emission inventories, using the 'folded retroplume technique'. For this, a footprint layer that contains the emissions is defined. Since the case study is carried out in the cold season, levoglucosan emissions originate mainly from domestic heating with firewood. The result of the folding is a data field that describes the contribution of individual upwind domestic heating sources to the receptor. Adding up all contributions, the concentration at the receptor is obtained. When releasing two isotope tracers ^{12}LG and ^{13}LG , $\delta^{13}\text{C}$ can be calculated at the receptor. These modeling results can be compared with isotopic- and concentration measurements at the sampling sites. A closure study between modeling and measurements validates the modeling and leads to a better understanding of sources and processes of biomass burning aerosol.

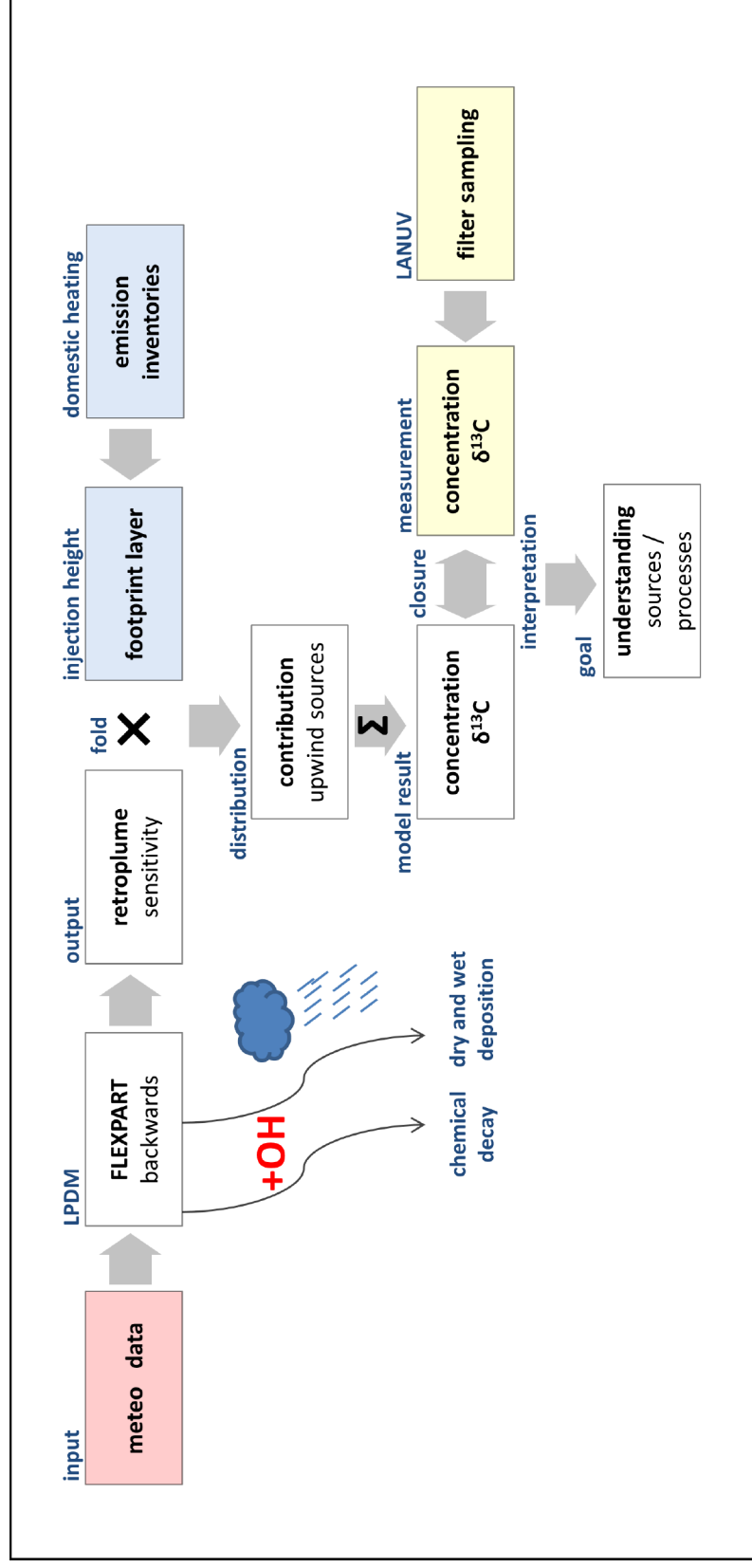


Figure 1.7.: Method overview. For elaboration, see Text.

2. FLEXPART modeling

The LPDM FLEXPART was first released in 1998 to model the mid- to long range transport and dispersion of pollutants from point sources. By now, fields of applications also cover accidents at nuclear power plants and water cycle or troposphere-stratosphere exchange modeling. The model was validated in various studies on the impact and quantification of transboundary pollution at downwind sites, e.g. Stohl et al. [1998], Stohl et al. [2002], Stohl et al. [2003]. The Fortran 95 source code is available under GNU general public license¹. FLEXPART Version 9.0 is used in this study, except for runs with the new wet deposition module which is part of Version 10.2beta. In this work, FLEXPART is only run in the backwards mode. The modeling process for this study is depicted in Figure 2.1.

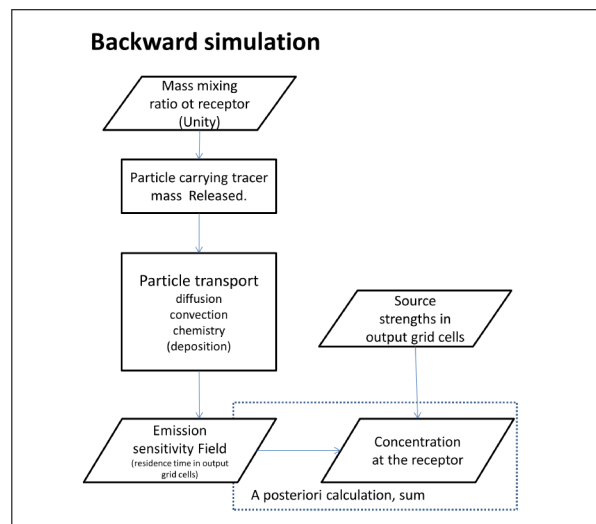


Figure 2.1.: Schematic description of the backwards modeling process. Particles are released at the receptor. The calculation of particle transport and diffusion is done several times with short time steps. The obtained sensitivity field is a posteriori folded with emissions to obtain the concentration at the receptor.

¹The source code is available online under www.FLEXPART.eu.

2. FLEXPART modeling

2.1. Model description

If not otherwise noted, the model description is based on Stohl et al. [2010].

Meteorological input data. FLEXPART uses wind fields from the European Centre for Medium-Range Weather Forecasts (ECMWF) or the Global Forecast System (GFS) in gridded binary (GRIB) format. Five three-dimensional fields are required as input: horizontal and vertical wind components, temperature and specific humidity. Additionally, 13 two-dimensional input fields are needed: surface pressure, total cloud cover, 10 m horizontal wind components, 2 m temperature and dew point temperature, large scale and convective precipitation, sensible heat flux, east/west and north/south surface stress, topography, landsea-mask and subgrid standard deviation of topography. The resolution is $1^\circ \times 1^\circ$ on 60 vertical levels with a time resolution of one hour.

Particle transport and dispersion. The trajectory equation is solved numerically to calculate the particle movement.

$$\frac{d\mathbf{X}}{dt} = \mathbf{v}[\mathbf{X}(t)] \quad (2.1)$$

The model wind \mathbf{v} in this equation consists of the grid scale wind $\bar{\mathbf{v}}$, the turbulent wind \mathbf{v}_t and mesoscale wind fluctuations \mathbf{v}_m .

$$\mathbf{v} = \bar{\mathbf{v}} + \mathbf{v}_t + \mathbf{v}_m \quad (2.2)$$

Only $\bar{\mathbf{v}}$ can be retrieved directly from the meteorological input data. \mathbf{v}_t is parametrized assuming a Markov process, based on the Langevin equation.

$$dv_{t_i} = a_i(\mathbf{x}, \mathbf{v}_t, t) dt + b_{i,j}(\mathbf{x}, \mathbf{v}_t, t) dW_j \quad (2.3)$$

Here, a_i is a drift term and $b_{i,j}$ a diffusion term, parametrized via input quantities such as air density and mean wind standard deviation. dW_j are uncorrelated, Gauss distributed random numbers that describe a Brownian motion with mean zero and variance dt .

\mathbf{v}_m closes the spectral gap between the grid scale wind velocities and the turbulent motion. The fluctuations can influence the dispersion of a particle plume significantly. They are parametrized assuming that grid scale wind variances contain information on subgrid wind variances.

2.1. Model description

A zero acceleration scheme is used to solve Equation 2.1 for \mathbf{v}_m and \mathbf{v}_t . It is accurate to the first order.

$$\mathbf{X}(t + \Delta t) = \mathbf{X}(t) + \mathbf{v}(\mathbf{X}(t)) \cdot \Delta t \quad (2.4)$$

For $\bar{\mathbf{v}}$ on the other hand, the truncation error of using a first order scheme can be significant. So here the particle position is corrected with an implicit two step method which is correct to the second order (Petterssen [1940]).

$$\mathbf{X}(t + \Delta t) = \mathbf{X}(t) + \frac{1}{2} \left[\mathbf{v}(\mathbf{X}(t)) + \mathbf{v}(\mathbf{X}(t + \Delta t)) \right] \cdot \Delta t \quad (2.5)$$

Lifting by moist updrafts in convective clouds is an effective transport mechanism in the troposphere. It is not resolved by the grid scale wind. The convective parametrization scheme by Emanuel and Živković Rothman [1999] is used in FLEXPART. Moist convection occurs if an air parcel fulfills

$$T_{vp}^{LCL+1} \geq T_v^{LCL+1} + \delta T, \quad (2.6)$$

where T_{vp}^{LCL+1} is the virtual potential temperature of the air parcel lifted to the model level above the lifting condensation level, T_v^{LCL+1} is the virtual temperature of its environment lifted to the same level and $\delta T = 0.9 K$ is the required excess temperature. Moist convection redistributes particles in the whole vertical column, so the moist convection scheme outputs a redistribution matrix with probabilities for displacements to the different heights. The well-mixed criterion is fulfilled which states that if a tracer is well mixed in an atmospheric column, it will stay that way after the convection.

Mixing layer. In the mixing layer of FLEXPART, tracers are mixed effectively, even at stable conditions. Vertical turbulence is added, in contrast to the free troposphere where only horizontal turbulent disturbances are considered. A shorter time step for the integration of Equation 2.1 is used than in the free troposphere. The mixing layer extends from the ground level to the mixing height which is parametrized from the grid scale data. It is set to the height where the Richardson number Ri exceeds the critical value of 0.25 (Stull [2001]).

$$Ri = \frac{(g/\Theta_0)(\Theta - \Theta_0)(z - z_0)}{(u - u_0)^2 + (v - v_0)^2 + 100 u_*^2} \quad (2.7)$$

Here, Θ_0 and Θ are the virtual potential temperatures at the surface level and at the current level, z is the height, u , v the wind velocities and u_* the roughness length.

2. FLEXPART modeling

Chemical processing. FLEXPART models OH-radical loss by reducing the tracer mass a particle carries.

$$m(t + \Delta t) = m(t) \cdot e^{-k \cdot [OH] \cdot \Delta t} \quad (2.8)$$

Here, m is the tracer mass, k is the OH-reaction constant and $[OH]$ is the OH concentration. A monthly averaged OH field with a resolution of $3^\circ \times 5^\circ$ from the GEOS-CHEM model (Bey et al. [2001]) is used. The temperature dependence of the reaction constant is taken into account.

Dry deposition. The dry deposition velocity v_d for aerosols in the constant flux layer is calculated by

$$v_d = \frac{1}{r_a(z) + r_b + r_a(z) r_b v_g} + v_g, \quad (2.9)$$

where $r_a(z)$ is the aerodynamic resistance and r_b is the quasilaminar sublayer resistance. The settling velocity v_g is calculated from the aerosol mass density ρ_d and diameter d_p .

$$v_g = \frac{g \rho_p d_p^2 C_{cun}}{18 \mu} \quad (2.10)$$

Here, g is the gravitational acceleration, C_{cun} the Cunningham slip-flow correction and μ is the dynamic viscosity of air. Besides being important to calculate the dry deposition velocity, the settling velocity also changes the particles trajectory.

Wet deposition. A new wet removal scheme for deposited mass in the backwards mode for the FLEXPART Version 10.2beta² was introduced by Grythe et al. [2017] and Eckhardt et al. [2017]. It uses cloud water fields from the ECMWF meteorological input data, differencing between below-cloud and in-cloud scavenging.

Nucleation scavenging occurs if a particle is in the precipitating fraction of a grid cell, at altitudes where cloud water is present. The scavenging coefficient Λ is determined by

$$\Lambda = F_{nuc} \frac{I}{PCW} i c_r, \quad (2.11)$$

where F_{nuc} is the nucleation efficiency, I is the fraction of the aerosol that is activated as a condensation nucleus, PCW is the precipitating cloud water and $i c_r$ represents the cloud water replenishment rate. F_{nuc} is tracer specific for water and ice condensation respectively.

²The new wet deposition module is still in the development stage. It is currently available under git@git.nilu.no: flexpart/flexpart.git, dev branch. Access December 13th 2018.

2.1. Model description

Impaction scavenging occurs below a precipitating cloud. Falling raindrops or snow flakes may collide with aerosol particles (probability: $P_{collision}$) and scavenge them if they attach to each other ($P_{coalescence}$). Thus the collection efficiency ($P_{collection}$) yields

$$P_{collection} = P_{collision} \cdot P_{coalescence} . \quad (2.12)$$

$P_{collision}$ is parametrized via the aerosol size and density specified by the user, the raindrop/snowflake size, fall speed etc. $P_{coalescence}$ is a tracer specification that depends on the microphysical properties of the aerosol.

Backwards mode. A detailed theoretical derivation of the source receptor relationship in trajectory based LPDMs in the backwards mode is given by Seibert and Frank [2004]. Atmospheric trace substances are affected by advection, diffusion, convective mixing, deposition and chemical reactions. Of these, only higher order chemical reactions can be nonlinear. If only first order chemical reactions like OH-decay are considered, chemical processing is a linear process as well. Thus the source receptor relationship can be described as a source receptor matrix \mathbf{M} with elements m_{ij} :

$$m_{ij} = \frac{y_j}{x_i} \quad (2.13)$$

Where y_j are the receptors and x_i are the sources.

The mass mixing ratio χ [kg/kg] of a particle can be affected by a source \dot{q} [$\text{kg m}^{-3} \text{s}^{-1}$] or a linear process α [s^{-1}]. There are no advective changes because the frame of reference moves with the particle.

$$\frac{d\chi(t)}{dt} = \frac{1}{\rho(t)} \dot{q}(t) + \alpha(t) \chi(t) \quad (2.14)$$

This equation has the analytic solution at the location \mathbf{x}^* and time t

$$\chi(\mathbf{x}^*, t) = \chi_0 \exp\left(-\int_0^t \alpha[\mathbf{x}(t'), t'] dt'\right) + \int_0^t \frac{\dot{q}[\mathbf{x}(t'), t']}{\rho[\mathbf{x}(t'), t']} \exp\left(-\int_{t'}^t \alpha[\mathbf{x}(t''), t''] dt''\right) dt' , \quad (2.15)$$

where χ_0 is the initial mass mixing ratio or background concentration at time $t=0$. A dimensionless transmission function p gives the mass fraction of a source which is transmitted along the trajectory to the receptor.

$$p(t') = \exp\left(-\int_{t'}^t \alpha[\mathbf{x}(t''), t''] dt''\right) \quad (2.16)$$

2. FLEXPART modeling

Thus Equation 2.15 becomes

$$\chi(\mathbf{x}^*, t) = \chi_0 p(0) + \int_0^t \frac{\dot{q}(t')}{\rho(t')} p(t') dt'. \quad (2.17)$$

Usually, many model particles arrive at the receptor in a certain time interval. Thus a temporal mean over the sampling time yields the mass mixing ratio at the sampling point.

$$\bar{\chi}(t_1, t_2) = \frac{1}{t_2 - t_1} \int_{t_1}^{t_2} \chi(\mathbf{x}^*, t) dt \quad (2.18)$$

Furthermore, in a numerical model Equation 2.17 is discretized.

$$\bar{\chi} \approx \overline{\chi_0 p(0)} + \frac{1}{J} \sum_j \sum_i \sum_n \left(\frac{\dot{q}_{in}}{\rho_{in}} p_{jn} \Delta t'_{ijn} \right) \quad (2.19)$$

Here J is the number of arrival time steps considered, j the arrival time index and i the spatial grid index. The time steps of the particle movement (t') are indexed with n . $\Delta t'_{ijn}$ denotes the residence time of the trajectory (arrival time j) in the grid cell (in), so it is also an indicator of the particle movement. The source function \dot{q}/ρ is not dependent on the arrival time j , so the equation can be rewritten as

$$\bar{\chi} \approx \overline{\chi_0 p(0)} + \sum_i \sum_n \left[\frac{\dot{q}_{in}}{\rho_{in}} \frac{1}{J} \sum_j (p_{jn} \Delta t'_{ijn}) \right], \quad (2.20)$$

which yields the source receptor relationship for a source at space i and trajectory time n .

$$\frac{\partial \bar{\chi}}{\partial \dot{q}_{in}} = \frac{1}{J} \sum_j \frac{p_{jn} \Delta t'_{ijn}}{\rho_{in}} \quad (2.21)$$

This derivation holds for mass mixing ratios χ [kg/kg] only. In this study, a tracer concentration c [ng/m³] is required. The source receptor relationship is calculated in the model by taking into account the air density ρ_{in} along the trajectory and at the sampling point. Equation 2.21 then becomes

$$\frac{\partial \bar{c}}{\partial Q_{in}} = \frac{1}{J} \sum_j p_{jn} \Delta t'_{ijn}. \quad (2.22)$$

In this study, the source ∂Q_{in} is given in [ng m⁻³ s⁻¹]. Equation 2.22 shows that a retroplume obtained by a backwards run for concentrations contains transmission corrected atmospheric residence times $p_{jn} \Delta t'_{ijn}$ [s].

2.2. Folded retroplume technique

FLEXPART retroplumes can be linked with emission inventories using the folded retroplume technique which was developed by Owen and Honrath [2009]. To obtain the contribution of different sources to the receptor, the emission rates in the respective grid cells are multiplied with the sensitivity of the receptor to that source. The sum of all contributions yields the concentration at the receptor.

$$\frac{\partial \bar{c}}{\partial Q_{in}} \cdot Q_{in} = \bar{c}_{in} \quad \Rightarrow \quad \sum_{in} \left(\frac{\partial \bar{c}}{\partial Q_{in}} \cdot Q_{in} \right) = \bar{c} \quad (2.23)$$

Emission inventories have to be available as gridded data with the same dimension as the retroplume. The 'folding' is thus the Hadamard product of two matrices with the same dimension. The grid cells where a source is present is termed the footprint layer of the emission. By adding up the contribution of all folded grid cells, the concentration at the receptor is obtained. The folding of model output with emissions is done a posteriori which has the advantage that different emission scenarios can be applied without rerunning the model.

Footprint layer of levoglucosan emissions. To apply the folded retroplume technique, emissions have to be available as a gridded footprint layer with the same dimension as the model output. Since this information is not available, taking into account that only wood combustion in the residential sector contributes to the collected levoglucosan in this winter time study, an approach was conceived, involving information on population densities, specific consumption of firewood in the investigated regions etc. For simplicity, in this approach description only the units are given.

A data set from the United Nations³ provides the firewood consumption of every European country per year.

$$[m_{firewood}^3 y^{-1}] \quad (2.24)$$

This is divided by the total population of the respective country to obtain the consumption per capita.

$$\Rightarrow [m_{firewood}^3 y^{-1}] / [\Sigma persons] = [m_{firewood}^3 person^{-1} y^{-1}] \quad (2.25)$$

³Firewood combustion data is obtained from statistical databases provided by the United Nations: data.un.org/Data.aspx?d=EDATA&f=cmlID%3aFW%3btrID%3a1231, access March 10th 2017.

2. FLEXPART modeling

The amount is weighted with the population density⁴.

$$\Rightarrow [\text{m}_{\text{firewood}}^3 \text{ person}^{-1} \text{ y}^{-1}] \cdot [\text{person km}^{-2}] = [\text{m}_{\text{firewood}}^3 \text{ km}^{-2} \text{ y}^{-1}] \quad (2.26)$$

The firewood volume consumption is converted to [kg] using a conversion factor of $500 \pm 200 \text{ kg}_{\text{firewood}} \text{ m}^{-3}$ (Döring et al. [2016]). Furthermore, the consumption is weighted with individual factors⁵ for every month, to describe seasonal variability in the wood consumption.

$$\Rightarrow [\text{m}_{\text{firewood}}^3 \text{ km}^{-2} \text{ y}^{-1}] \cdot [\text{kg}_{\text{firewood}} \text{ m}_{\text{firewood}}^{-3}] = [\text{kg}_{\text{firewood}} \text{ km}^{-2} \text{ y}^{-1}] \quad (2.27)$$

The levoglucosan emission is derived by using an average emission factor of 200 mg levoglucosan per kg firewood (Fine et al. [2002]).

$$\Rightarrow [\text{kg}_{\text{firewood}} \text{ km}^{-2} \text{ y}^{-1}] \cdot [\text{mg}_{\text{LG}} \text{ kg}_{\text{firewood}}^{-1}] = [\text{mg}_{\text{LG}} \text{ km}^{-2} \text{ y}^{-1}] \quad (2.28)$$

Converting time and spatial extend to SI units yields

$$\Rightarrow [\text{mg}_{\text{LG}} \text{ km}^{-2} \text{ y}^{-1}] / [\text{m}^2 \text{ km}^{-2}] / [\text{s y}^{-1}] = [\text{mg}_{\text{LG}} \text{ m}^{-2} \text{ s}^{-1}]. \quad (2.29)$$

The domestic heating emission enters the atmosphere as a hot plume of wood smoke with an injection height of 100 m - 300 m (Zhang et al. [2014]). This footprint layer contains the volume emission needed for the folding.

$$\Rightarrow [\text{mg}_{\text{LG}} \text{ m}^{-2} \text{ s}^{-1}] / [\text{m}] = [\text{mg}_{\text{LG}} \text{ m}^{-3} \text{ s}^{-1}] \quad (2.30)$$

Multiplying this term with the transmission corrected residence time obtained from a FLEXPART model run like in Equation 2.23, the contribution of the grid cell to the concentration at the receptor is obtained.

$$\Rightarrow [\text{mg}_{\text{LG}} \text{ m}^{-3} \text{ s}^{-1}] \cdot [\text{s}] = [\text{mg}_{\text{LG}} \text{ m}^{-3}] \quad (2.31)$$

The background levoglucosan [ng/m^3] is considered constant during the runs. It is added during the folding step. The result might be errornous due to simplifications and uncertainties in every step. This issue is discussed in the sensitivity studies (Chapter 3).

⁴Population density data is obtained from the NASAs web page:
neo.sci.gsfc.nasa.gov/view.php?datasetId=SEDAC_POP, access February 6th 2017.

⁵Monthly weighting is estimated from a personal survey.

2.2. Folded retroplume technique

From concentrations to isotopic ratios. To fulfill the proposed tasks of this work, $\delta^{13}\text{C}$ must be given as a model output in addition to the concentration. The isotope ratio is obtained by introducing two isotope tracers ^{12}LG and ^{13}LG in the model. Similar to the approach of Stein and Rudolph [2007] and Gensch et al. [2011], the tracers differ only in their OH reactivity. Isotope ratios are obtained by folding the retroplumes of the two tracers from the resulting concentration ratio.

The model emissions of ^{12}LG and ^{13}LG must resemble the δ_0 -value the emission. Rearranging Equation 1.1, using an isotopic composition at the source δ_0 and the reference ratio⁶ R_{standard} yields

$$\left(\frac{\delta_0}{1000} + 1\right) \times R_{\text{standard}} = R_{0,\text{sample}} = \frac{^{13}\text{LG}_{0,\text{sample}}}{^{12}\text{LG}_{0,\text{sample}}} \quad (2.32)$$

This yields for the emissions

$$^{13}\text{LG}_0 = R_0 \cdot ^{12}\text{LG}_0. \quad (2.33)$$

During the model run, the relative loss of ^{13}LG is slightly lower than the loss of ^{12}LG . Similarly, the isotopic ratios $\delta^{13}\text{C}$ at the sampling sites can be calculated from the concentrations of the two released tracers.

$$\delta^{13}\text{C}_t = \left[\frac{^{13}\text{LG}_t / ^{12}\text{LG}_t}{R_{\text{standard}}} - 1 \right] \cdot 1000 \text{‰} \quad (2.34)$$

⁶Vienna Pedee Belemnite (VPDB) with $^{13}\text{C}/^{12}\text{C}_{\text{VPDB}} = 0.0112372$ (Craig [1957])

3. Sensitivity studies

Sensitivity studies were carried out by varying important parameters in the modeling process: driving meteorology, kinetic data for the reaction of levoglucosan with OH, deposition and heating behaviour of the population. The goal was to reveal the governing simulated processes and to assess the modeling performance.

For the footprint layer, emissions obtained as in Section 2.2 were used. An average source specific $\delta_0^{13}\text{C} = -24.0\text{‰}$ was used in the earliest runs (Sang et al. [2012]). ECMWF meteorology wind data was used. Ca. 200 000 model particles were gradually released at the sampling point during 24 hours of sampling. Levoglucosan was considered as a reactive tracer. For its oxidation by OH, a rate constant of $2.67 \times 10^{-12} \frac{\text{cm}^3}{\text{molec} \cdot \text{s}}$ and a KIE of 1.00229 (Sang et al. [2016]) were used. The model was run backwards for 7 days, which is at the highest range of the levoglucosan expected lifetime.

With this setup, retroplumes of the sampled aerosol were modeled as described in Section 1.4, showing the relative contribution of potential sources to the receptor. The ‘residence times’ of the investigated air masses for 19 January 2017 are plotted in Figure 3.1. Here, the most probable emissions are situated easterly of the Eifel station, close to the sampling point. Retroplumes were calculated for all samples, being depicted in the 10th column of the Overview Table in Appendix B.

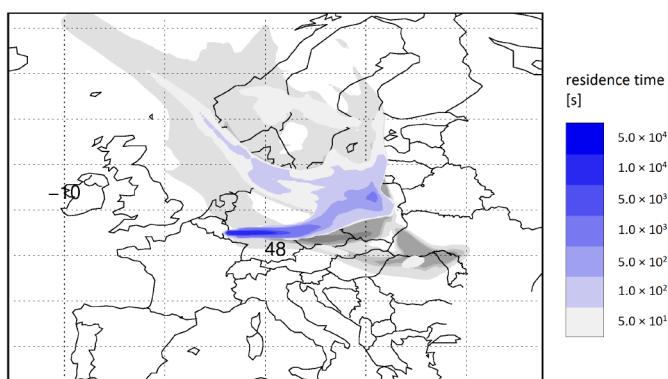


Figure 3.1.: Retroplume for sampling on 19 January 2017, Eifel station with residence time in the footprint layer (100 m-300 m, blue) and in the whole atmosphere (grey) on a logarithmic color scale.

For the sensitivity studies, the model parameters were successively varied. The changes of the output depending on the changes in the input parameters were evaluated for consistency. The optimal configuration was used for the case study described in Chapter 4.

3. Sensitivity studies

3.1. Driving meteorological input data.

Uncertainties in the driving meteorology are one of the major error sources in Lagrangian modeling (Davis and Dacre [2009], Lin [2013]). The spatial resolution of $1^\circ \times 1^\circ$ for meteorological data equates to a range of $100 \text{ km} \times 100 \text{ km}$ in mid-European latitudes. Angevine et al. [2014] showed that error propagation through FLEXPART induced by meteorological input data is not trivial. They estimated that ca. 30-40 % error of a folded retroplume is caused by this uncertainty.

GFS runs. In this study, the FLEXPART sensitivity to the meteorological input data was assessed by running the model with a Global Forecast System (GFS) dataset with 39 vertical levels, additional to the ECMWF runs.

A good agreement between the two meteorologies was found on 6 November 2015, at the Eifel station (Figure 3.2). Both general wind direction and mixing layer height are very similar. Oppositely, on 5 March 2016 at the Eifel station, the GFS plume points towards another source region, and shows quite different centroid trajectories and mixing height (Figure 3.3). In the GFS run, centroids are often below the mixing height in the last hours before sampling, which increases the concentration through uptake of fresh emissions. The modeling concentration and $\delta^{13}\text{C}$ results for the two days in are summarized in Table 3.1. The uncertainties in the mixing height determination are thus a cause of significant error, since it strongly influences the particle redistribution and influence of sources with low injection height.

Table 3.1.: Concentration and $\delta^{13}\text{C}$ obtained using different meteorologies.

6 November 2015 Eifel station (good agreement)	c [ng/m ³]	$\delta^{13}\text{C}$ [‰]	5 March 2015 Eifel station (bad agreement)	c [ng/m ³]	$\delta^{13}\text{C}$ [‰]
ECMWF	36.75	-23.34	ECMWF	46.76	-23.23
GFS	38.23	-23.35	GFS	129.19	-23.06

The results obtained using both meteorologies for all sampling days are summarized in Appendix B. The resulted concentrations and δ -values are generally very similar. Differences in the concentrations obtained with the two meteorologies are with few exceptions very low up to 10 %, which is in the measurement error range. Differences in the isotopic composition are below 0.5‰, which is the measurement error range. In the treatment of the mixing height and also in the general wind direction, no significant differences were registered for most modeling days. Both datasets are generally considered reliable, but due to its higher resolution, the ECMWF meteorology was chosen to initialize the model.

3.1. Driving meteorological input data.

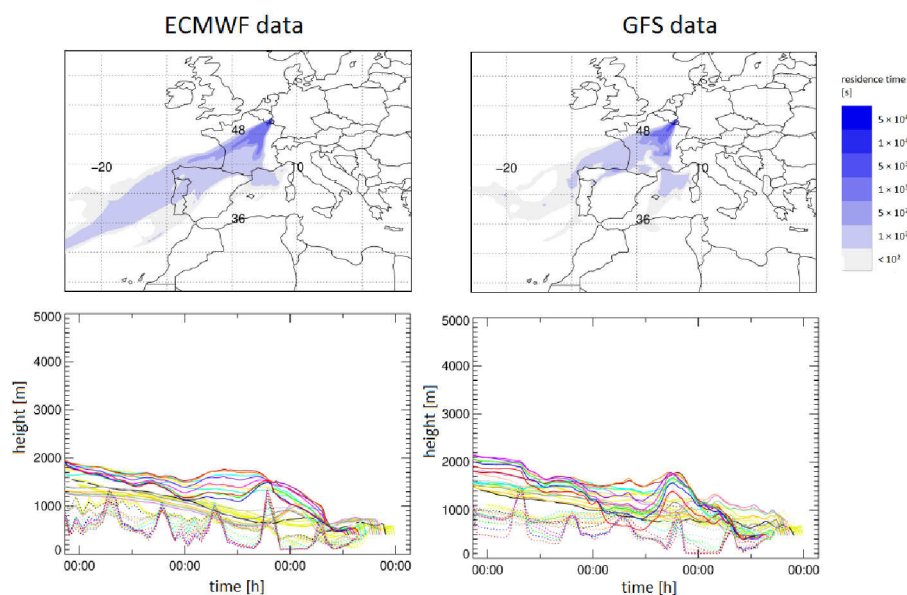


Figure 3.2.: Modeling results with good agreement for both meteorologies. 6 November 2015, Eifel station. Top: Retroplumes, Bottom: Centroid trajectories (solid) and the corresponding mixing layer height (dashed) for every release hour.

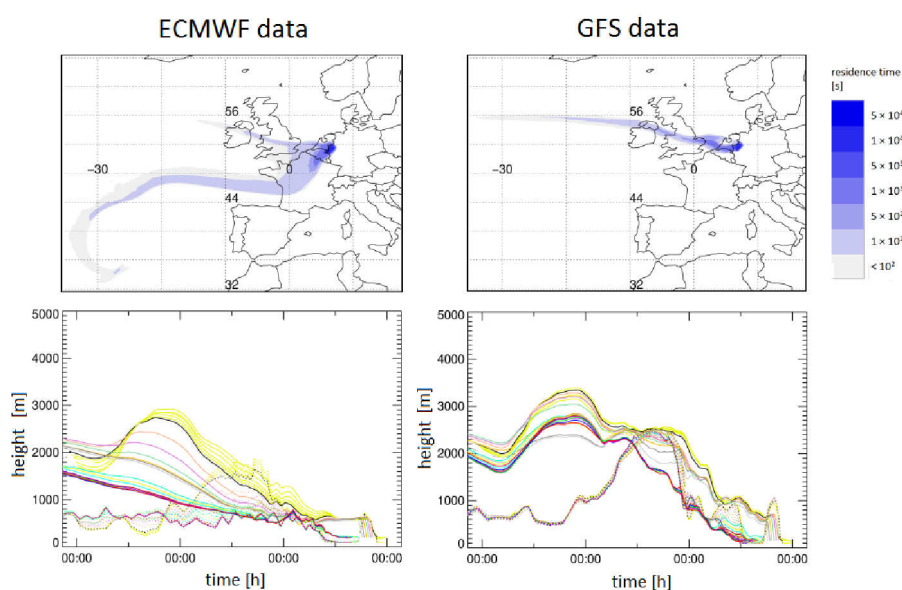


Figure 3.3.: Modeling results with high deviations between the two meteorologies. 5 March 2016, Eifel station. Top: The retroplumes show differences in the overall wind direction. Bottom: Centroid trajectories (solid) and the corresponding mixing layer height (dashed) show significant differences, which strongly affects the receptor sensitivity to the source. For GFS meteorology, the centroids are more time below the mixing height, which results in a higher concentration (Table 3.1)

3. Sensitivity studies

3.2. Chemical aging

In this Section, the influence of the chemical degradation by OH-radicals on the concentration and isotopic composition of the levoglucosan is assessed.

Age of sampled aerosol. To roughly estimate the age of the sampled aerosol, emissions were differentiated depending on their age when arriving at the receptor. Four age categories were defined: (i) emissions were injected into the model parcel during the last 24 h; (ii) the contributing emissions occurred between the last 24-48 h; (iii) emissions from 48-72 h (iv) the contributing emissions were older than three days. Based on that classification, for a run with typical aerosol age (1 April 2017, Eifel station), ca. 51 % of the sampled aerosol originates from the sampling day, 38 % from the day before, 7 % of the third day and only 4 % of the rest of the modeled period. Figure 3.4 shows emission contributions from the different days using a color code which is valid also for the rest of the simulated results, presented in the 12th column of Appendix B.

According to the model, the major part of the sampled aerosol originates from local emissions of the sampling day and the day before for most runs. Percentages of emission contribution for different days in the history of the model air parcels and related plots like Figure 3.4 are summarized in Appendix B. On average only ca. 6 % of the sampled aerosol is older than three days. This strongly indicates that chemical aging is no governing process for this study. Furthermore the original approach of backwards modeling the last 7 days turns out to be sufficient to comprise also remote sources.

OH concentration. The deployment of OH concentration in FLEXPART is described in Section 2.1. During the cold season, the concentration is low due to the low intensity of sunlight. OH concentration used in the model runs is in the range of $0.4 \times 10^6 \frac{\text{molec}}{\text{cm}^3}$, being a realistic average for the cold season in Europe. The OH concentration spatial distribution was not varied in a separate sensitivity study since only averaged data is of interest. A sensitivity study for the reaction constant k_{OH} was carried out further below.

In fact, levoglucosan is degraded by OH formed only during daylight time. Yet, by assuming a monthly mean OH-concentration, diurnal variations in the chemical decay are neglected in the simulations. For the isotopic composition this is no source of error, since the **average** OH concentration encountered by the model particles governs the change in the δ -value according to Equation 1.4. For the concentrations it is neither problematic because a full 24 h of sampling time provides a daily mean that mitigates the errors caused by using a mean OH-concentration.

Reaction constant. By varying k_{OH} , an estimate of the chemical decay on the modeling results was obtained. Runs with no chemical decay and with a higher reaction constant

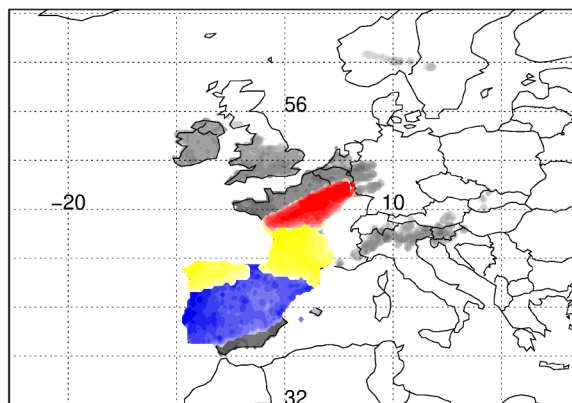


Figure 3.4.: Contributed levoglucosan emissions from different modeling days for 1 April 2017, Eifel station. The plot constrains source regions from the sampling day (red), the day before (yellow), the third day (blue) and the rest of the modeled period (grey).

from Hennigan et al. [2010] were carried out, additionally to the initial runs using the reaction rate constant from Sang et al. [2016]. The runs were conducted for 1 April 2017, because the sampled air masses of this day have a typical age for this study. The resulting concentrations and δ -values are summarized in Table 3.2.

Table 3.2.: Concentration and ^{13}C enrichment obtained with different reaction constants.

1 April 2017 Eifel station	c [ng/m ³]	aging [‰]
$k_{\text{OH}} = 0.0$	21.13	+0.00
$k_{\text{OH}} = 2.67 \pm 0.03 \times 10^{-12} \text{ cm}^3/\text{s}$ (Sang et al. [2016])	19.75	+0.25
$k_{\text{OH}} = 1.1 \pm 0.5 \times 10^{-11} \text{ cm}^3/\text{s}$ (Hennigan et al. [2010])	17.32	+0.43

Considering the reaction constant from Sang et al. [2016] results in a very small change in the concentration, which is not surprising, given the almost inexistent chemical aging of the sampled aerosol (see above). This would be totally different in the case of a significant chemical decay, such as during long range transport or strong OH exposure in summer. The use of the reaction rate constant found by Hennigan et al. [2010] induces a ca. 10% deviation in the concentration, which is in the range of the measurements error. The influence on the isotopic composition is below detection limit of ca. 0.5 ‰ for both reaction constants.

3. Sensitivity studies

The findings from this Section demonstrate that both concentration and isotopic composition at the sampling site are rather affected by mixing with sources than by chemical loss processes. This is consistent with D. Busby et al. [2015], who pointed out that levoglucosan is relatively stable during winter due to the low OH-concentration.

KIE. The uncertainty in the KIE determined by Sang et al. [2016] ($KIE = 1.00229 \pm 0.00018$) is low, compared to the variances in k_{OH} . According to Equation 1.4, the change of the isotopic composition due to OH-decay depends on the product $k_{OH} \cdot \epsilon_{OH}$. This renders a sensitivity study for the KIE unnecessary.

3.3. Deposition

Other than the slow chemistry in winter, loss processes by deposition might strongly influence the concentration and isotopic composition in the model. To assess their significance, a sensitivity study was carried out by running the model with the deposition modules switched off and on.

Wet deposition. A 'wet deposition' run was carried out for the sample collection on December 12, 2015. This day was picked to show maximum wet scavenging impact, because meteorological data indicated precipitation occurring at the sampling day¹. For that, the new wet deposition module was implemented with tracer specifications based on Saarnio et al. [2010] and Cozic et al. [2007]. The bulk mass of fresh biomass burning aerosol emissions was defined to be in the accumulation mode, described by a lognormal size distributions with mean $0.2 \mu\text{m}$ and $\sigma = 0.1 \mu\text{m}$. The aerosol particle density was considered 1.4 g/m^3 and $P_{coal,rain} = P_{coal,snow} = 1.0$.

Table 3.3.: Concentration influenced by wet deposition

8 December 2015 EIFEL station	c [ng/m ³]
measured	70.23
modeled	130.20
modeled, with wet depo	84.13

The results presented in Table 3.3 show that wet deposition is a considerable sink for biomass burning aerosol, and can be described well by FLEXPART in the backwards mode. There are

¹Precipitation data is available on the web page <http://wetter3.de/>, access February 1th 2019.

no occurrences of in-cloud scavenging in the model. This is consistent with Reid et al. [1998], who pointed out that anthropogenic emissions in the mixed layer do not influence the formation of clouds due to the low injection height.

In Appendix B, the 'info'-column indicates whether there exist unresolved sinks, and whether precipitation occurred in the modeled period. Although a high sensitivity of concentration to wet deposition is found, the case study (Chapter 4) was performed without wet deposition, because to include it routinely in the runs, some further adjustments of FLEXPART Version 10.2beta are necessary. Wet deposition has no direct influence on the isotopic composition of the sampled aerosol due to the predominance of the local sources. This would be totally different in case 'aged' aerosol would be removed by precipitations, resulting in an overall δ -value decrease.

Dry deposition. Gravitational settling is switched off in FLEXPART when the model is initialized with more than one tracer because it may affect the particle trajectory differently for different species. So a direct simulation of all dry deposition effects on isotope ratios is not possible.

To test the influence on the concentration, the aerosol particles were implemented with the same properties as in the wet deposition sensitivity study. A coarse mode with mean $6\ \mu\text{m}$ was added. This mode is formed by aged biomass burning aerosol that partly coagulates with coarse mode aerosol from other sources (Saarnio et al. [2010]).

Table 3.4.: Concentration affected by dry deposition exemplary for 1 April 2017.

1 April 2017 Eifel station	settling velocity [m/s]	loss [%]
No settling	0.0	0.00
$\bar{d} = 0.2\ \mu\text{m}$	-1.35×10^{-4}	3.96
$\bar{d} = 6.0\ \mu\text{m}$	-0.12	22.19

The results in Table 3.4 show that dry deposition does not affect the concentration of fresh aerosol in the accumulation mode significantly. Thus dry deposition is no considerable sink for this study because most of the sampled aerosol is about one day old (Section 3.2). For aged coarse mode particles, dry deposition is an important loss process. Dry deposition affects the isotopic composition when removing aged aerosol, similar to the effect described above.

3. Sensitivity studies

3.4. Folding receptor sensitivities to source regions with biomass burning emissions

In this Section, the implementation of levoglucosan emissions from residential firewood combustion is described in detail, pointing out source of biased results due to missing information on source strength and characterization.

Source distribution. Generally, the demand for reliable emission inventories for atmospheric pollutants is big. Knowledge on levoglucosan originating from residential heating is not existing. Therefore, in this work, an approach was developed to estimate these emissions from available data (Section 2.2). There are several sources of uncertainty arising from potential spatial and temporal variability of the emission intensities. Apart from domestic heating, outdoor fires might contribute as well to the biomass burning aerosol burden. FIRMS fire inventories² show no major fire events in Europe during the considered periods. Large-scale fire events occur usually during the warm season. Small-scale outdoor fires might contribute to the background aerosol burden in winter (see below).

The firewood consumption and population density data (Equations 2.24 to 2.26) are gained from the UN³ and the NASA⁴ respectively. Systematic errors are caused from seasonal and regional differences in the wood acquisition and consumption. By considering the monthly mean⁵ of the firewood consumption, weekly to diurnal variances in the emissions are neglected. Weighting with the population density is not representative for the real spatial distribution of the wood consumption. E.g. in cities with high population density, fireplace heating is rather unusual. There exist studies that divide living areas into the different categories 'city', 'suburbs', 'close to a city' and 'rural' (Döring et al. [2016]) or address wood stove exhaust down to the single chimney (Baumbach et al. [2010]), but this is beyond the scope of an Europe-wide study.

The emitted levoglucosan quantity is proportional to both conversion factors in the Equations 2.27 and 2.28. The uncertainty of the factor $(500 \pm 200) \text{ kg}_{\text{firewood}}/\text{m}^3$ (Döring et al. [2016]) results from different densities of woods used in Europe. The conversion factor from wood weight to levoglucosan emission depends on the wood type and the combustion process. It was determined for different set-ups by Schauer et al. [2001], Fine et al. [2004] and Jimenez et al. [2017]. Some studies detected very high levoglucosan quantities per wood burned that increase the mean value significantly. A good estimated conversion factor is $(200 \pm 100) \text{ mg}_{\text{LG}}/\text{kg}_{\text{firewood}}$.

²Fire Information for Resource Management System (FIRMS), a NASA product. firms.modaps.eosdis.nasa.gov, access January 10th 2019

³Firewood consumption by UN data: data.un.org, access March 10th 2017.

⁴Population density data by NASA: neo.sci.gsfc.nasa.gov, access February 6th 2017.

⁵Monthly weighting is estimated from a personal survey.

3.4. Folding receptor sensitivities to source regions with biomass burning emissions

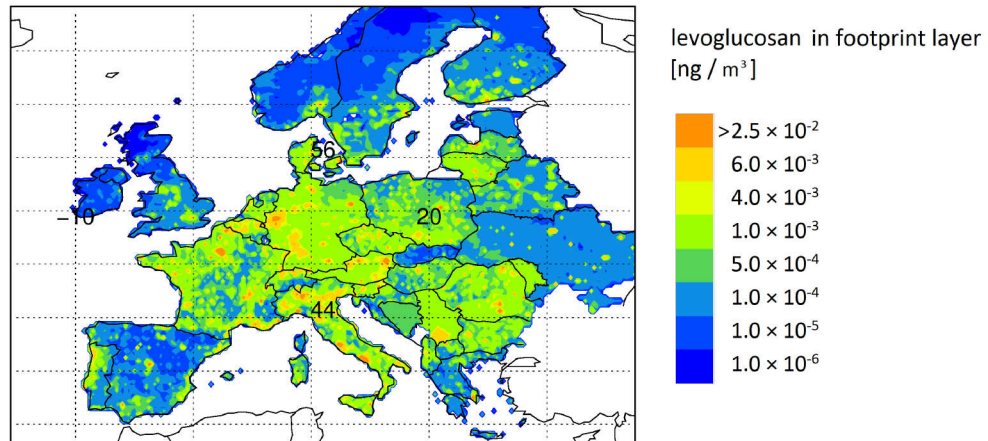


Figure 3.5.: Emissions of levoglucosan into the footprint layer (100 m - 300 m) in Europe for January.

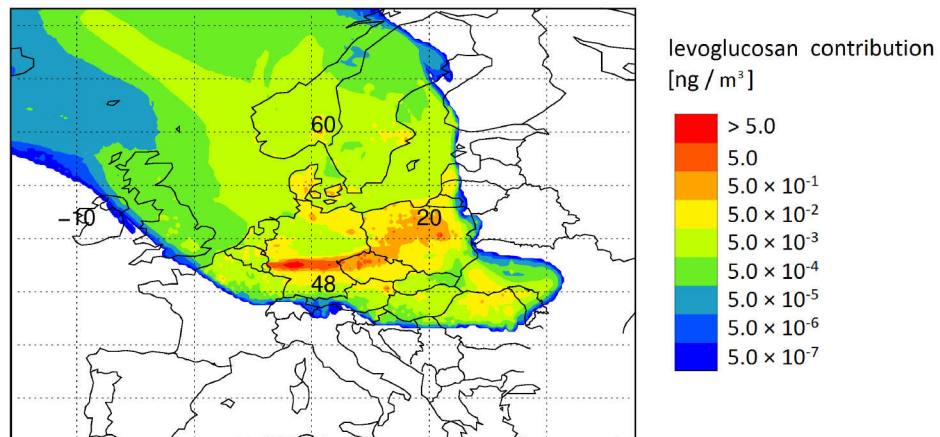


Figure 3.6.: Retroplume of 19 January 2017 (Figure 3.1), folded with emissions in Figure 3.5 on a logarithmic color scale. For this day, the source regions were, as already expected from the un-folded retroplume in eastern direction.

3. Sensitivity studies

Properties of the footprint layer. The injection height of a fire emission results from its temperature-affected ascent. It is usually parametrized via extent and temperature of the exhaust. Unlike large outdoor fires, woodstoves for home use are quite similar in these properties. According to Zhang et al. [2014], the footprint layer for domestic heating emissions stretches from 100 m - 300 m.

The model results are not sensitive to the footprint layer height as long as it is inside the mixing layer of FLEXPART where emissions are effectively mixed (Hüser et al. [2017]). This is valid for the modeled period because mixing heights are mostly above 1000 m during day and drop only occasionally below 300 m during night. Furthermore, increasing the thickness of the footprint layer has no major influence on the model outcome because of two counteracting effects. A greater dilution reduces the impact of a source, yet a wider spread of the emission increases the residence time of model particles in the footprint layer.

The levoglucosan present in the footprint layer is depicted in Figure 3.5. The retroplume of 19 January 2017, folded with these emissions is depicted in Figure 3.6. Plots of folded retroplumes for all sampling days are summarized in the 10th column of Appendix B.

Temporal variability of emissions. Assuming after hour domestic heating only from 5 pm to 10 pm changes the concentration less than 10 % for most days which is below detection limit. Since the sampling occurs during a full 24 hours and especially the spatial distribution of the sources favours averaging, a possible diurnal variability of emissions was neglected in this study. See Appendix B for individual results.

3.5. Summary

This sensitivity analyses have conclusively demonstrated that different meteorologies brought in few cases significant variations in the results. For this winter study, chemical degradation is not expected. Therefore varying the kinetic data would not influence the outcome of the model runs significantly. As expected, the consideration of wet deposition may change the obtained concentrations, whereas dry deposition is no important sink for coalgulation mode aerosol. For the isotopic ratios, the aerosol deposition loss is no major influence, since local sources play a major role.

Based on these findings, an optimal model configuration was set and used for the following case study: The case study was carried out with ECMWF driving meteorology. Levoglucosan was implemented as a reactive tracer with $2.67 \times 10^{-12} \frac{\text{cm}^3}{\text{molec} \cdot \text{s}}$ and a KIE of 1.00229 (Sang et al. [2016]). Deposition was not yet included in all runs, but special attention must be drawn to days with precipitation. The derived levoglucosan emission from domestic heating with firewood was used.

4. Case study

Domestic heating with firewood is increasingly popular in Germany. It is considered as 'clean' and nature friendly. Nevertheless, wood-fired oven exhaust recently became a concern due to the substantial amount of soot and fine dust emitted. There exist ca. 14 million small-scale furnaces in Germany, which produce fine dust in quantities equal to the total traffic exhaust (Amann et al. [2018]). A law change in 2010 (Verordnung über kleine und mittlere Feuerungsanlagen - 1. BImSchV) introduced new regulations for modernization requirements of wood-fuelled installations in private households. The local domestic heating exhaust is monitored by the environmental authorities in the respective municipalities. It is desired to investigate whether the sampled biomass burning aerosol burden is of local origin, or transported from afar. Aerosols of local origin can be mitigated by reducing local emissions, whereas remote contributions must be regulated on a national or even Europe-wide basis.

4.1. Ambient observations of levoglucosan concentration and isotope ratio

The present case study is carried out in collaboration with the Landesamt für Natur, Umwelt und Verbraucherschutz Nordrhein-Westfalen (LANUV). To mitigate the biomass burning aerosol burden in living areas, LANUV questions the contribution of local, regional and remote biomass burning sources to the aerosol burden in living areas. To investigate that, modeling was combined with ambient observations of levoglucosan concentration and isotopic ratios for a comprehensive understanding of biomass burning aerosol sources and fate in the atmosphere. It is expected that the biomass burning aerosol in the considered periods mainly originates from domestic heating with firewood (see Section 3.4).

Aerosol PM₁₀ fraction (particles with aerodynamic diameter smaller than 10 μm) is sampled on a regular basis on filters at stations belonging to the LANUV monitoring network at 24 h intervals. Two sampling sites with opposite characteristics were chosen for this study. One is an urban background station in Mülheim Styrum (‘STYR’ 51.453459°N, 6.86505°E). The other one is in a rural area in the Eifel, near the village of Simmerath (‘EIFE’ 50.653234°N, 6.281008°E). The filters are changed at 00:00 UTC+1. 25 days from the cold seasons of 2015-2017 were selected for this study. Preliminary back-trajectory calculations on these days indicate air mass origins from different wind directions to include various potential source regions. The quantity of the levoglucosan present on the filter material was determined at the LANUV. An overall measurement error of 11% was estimated. Isotopic analyses were carried out at

4. Case study

IEK-8, Forschungszentrum Jülich, by liquid extraction-thermal desorption-two dimensional gas chromatography, coupled with isotope ratio mass spectroscopy (LE-TD-2D-GC-IRMS, as used by Gensch et al. [2018]). All measurement results are summarized in Appendix B.

4.2. FLEXPART runs vs. ambient observations

FLEXPART was initialized as described in Chapter 3. Specific treatment of input data is given in the following. The retroplumes in Appendix B already give an idea of the respective source regions of the sampled aerosol.

Background aerosol. Due to a lack of data on the levoglucosan background concentration in the cold season in Europe, the lowest measured concentration (12.4 ng/m^3 on 10 November 2015 in the Eifel) serves as the input value for the simulations. It is added to the modeled concentration as a constant offset. Due to missing knowledge, fluctuations in the background concentration are neglected.

Concentration. Model output and measured concentrations are set side by side in Figure 4.1 (for details, see Appendix B). Generally, it can be seen that the simulation results and the observation are situated in the same range. For the rural background station (‘EIFEL’), the concentration is in some cases overestimated by the model. This indicates that there are most likely no unresolved sources. In the cases of overestimation, additional runs are necessary, where the wet deposition module is switched on (see Section 3.3).

Other than that, at the urban background station (‘MÜLHEIM-STYRUM’), model underestimations together with overestimations can be seen. This indicates that unknown individual sources close to the measuring station influence the local aerosol burden. These sources can be described by a local model (e.g. Baumbach et al. [2010]).

To emphasize the influence of wet deposition, days with precipitation¹ are plotted in blue in Figure 4.1, in contrast to the days with few or without precipitation which are plotted in red. High modeled concentration overestimation at the Eifel station often occurs on days with precipitation. For days with a low concentration, precipitation does not seem to be a source of error, presumably because of the sampling situation. For the urban station, precipitation can explain some overestimated concentrations. Nevertheless, here it is difficult to quantify wet scavenging vs. the influence of unresolved sources close to the receptor. Wet deposition runs are necessary to learn more about this topic.

¹Precipitation data is available on the web page <http://wetter3.de/>, access February 1th 2019.

4.2. FLEXPART runs vs. ambient observations

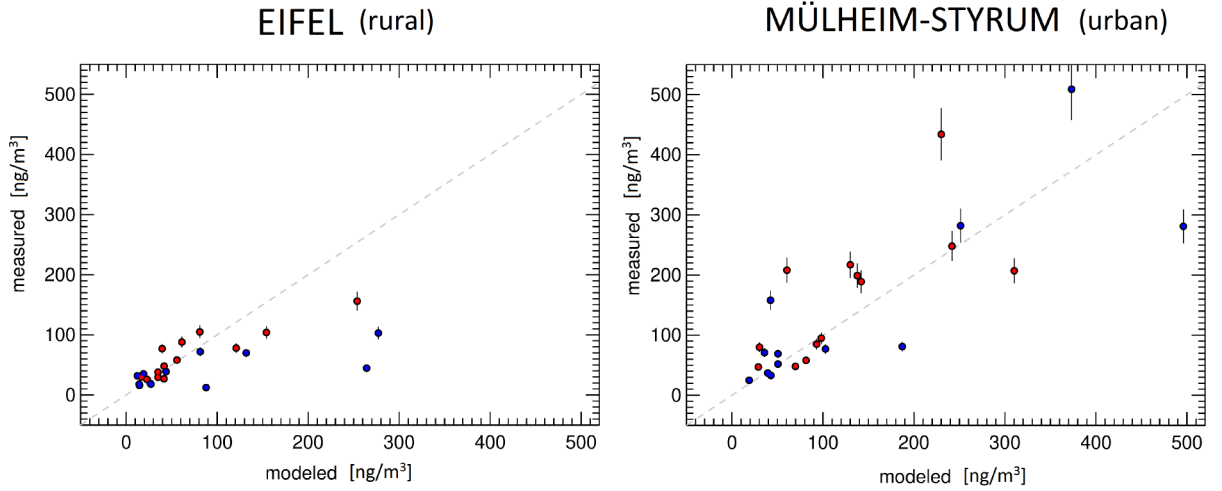


Figure 4.1.: Comparison between modeled and measured levoglucosan concentration in the Eifel and in Mülheim Styrum, and the 1:1 line (dashed). Days with precipitation are marked blue, days without precipitation are marked red. The measurement uncertainty is 11 %.

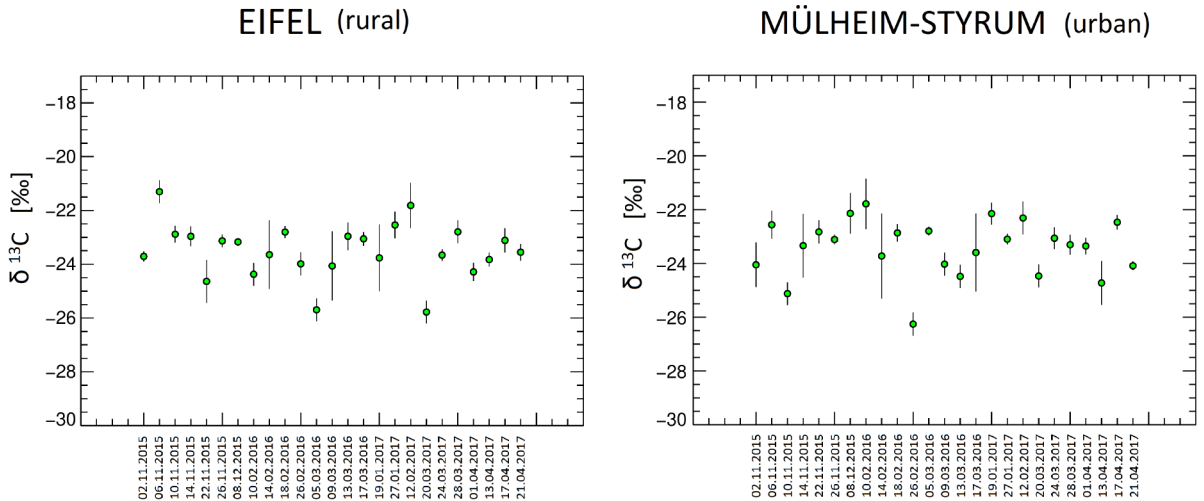


Figure 4.2.: $\delta^{13}\text{C}$ of the sampled levoglucosan for both measurement stations, including uncertainties. The x-axis is labeled with the respective sampling days.

4. Case study

Isotopic measurements. Figure 4.2 shows the measured δ -values of the sampled levoglucosan for both measurement stations (see Appendix B for individual values). The isotopic composition ranges between -26.3 ‰ and -21.3 ‰. There are two possible explanations for this significantly high variance: (i) very different sources with different isotopic ratios, or (ii) different aerosol chemical aging.

The findings of the chemical aging sensitivity study (Section 3.2) show that processing by OH has no major influence on the isotopic composition in this winter study. Most of the sampled aerosol is about one day old. Furthermore, chemical decay by such low OH concentrations in the cold season is insignificant. Thus mixing of sources characterized by various isotopic composition might explain the observations.

Keeling plots. In absence of chemical reactions, the isotopic ratios plotted vs. the inverse concentration is expected to give insight in the mixing of two levoglucosan reservoirs, in this case fresh emission and background (Figure 4.3). The sampled levoglucosan originates from local sources, characterized by high levoglucosan concentrations.

A linear regression analysis was carried out. The obtained y-intercept was calculated to be -23.20 ± 0.08 ‰. This value represents a good guess for the isotope ratio of the fresh emissions. The fitted line to the experimental data is almost parallel to the x-axis (slope: -9.79 ± 3.31), indicating that the isotopic composition of the background aerosol is not very different from that of the emissions. The 95 % confidence band well encloses the fitted line, supporting the statistical significance of the regression analysis. The 95 % prediction interval comprises with 95 % probability all measured data points. The interval maximum and minimum curves yield y-intercept values of -25.3 to -21.4 ‰. These values, representing the most probable source isotopic ratio of the investigated aerosol correspond well with the isotopic composition measured in aerosol from the combustion of several C3 plants (Sang et al. [2012]) within error ranges. It can also be concluded that the variability in the observed δ -values is due to the contribution of local sources characterized by very different isotopic ratios in the above mentioned range.

Since there is a lack of data on this topic, the model runs were initialized with an emission δ -value of -23.20 ‰ and background lighter by 0.79 ‰, derived from the slope of the linear fit according to Equation 1.6. The simulation results are shown in Figure 4.4. See Appendix B for individual results.

The modeled δ -values are situated almost in all cases on the line fitted to the observations. Some values show 'aging' in the range of up to 0.25 ‰, which is a realistic isotopic fractionation during hours to a few days under winter conditions. Overall, this closure study shows good agreement between the model and observation. This shows that FLEXPART well describes the atmospheric processes investigated in this study. The unknowns, introducing biases in the analyses, remain a good description of the sources and background.

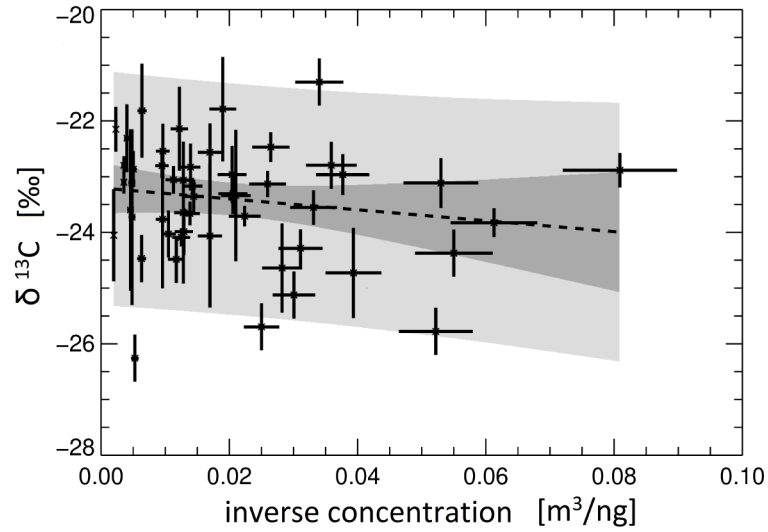


Figure 4.3.: Keeling plot of all LANUV samples. The linear fit is dashed black, its 95 % confidence interval is marked dark grey. The area that contains with 95 % confidence all measurements is marked light grey. The tendency shows a very weak influence of mixing with background aerosol, yet the y-intercept spread explains variances in the measured isotopic composition.

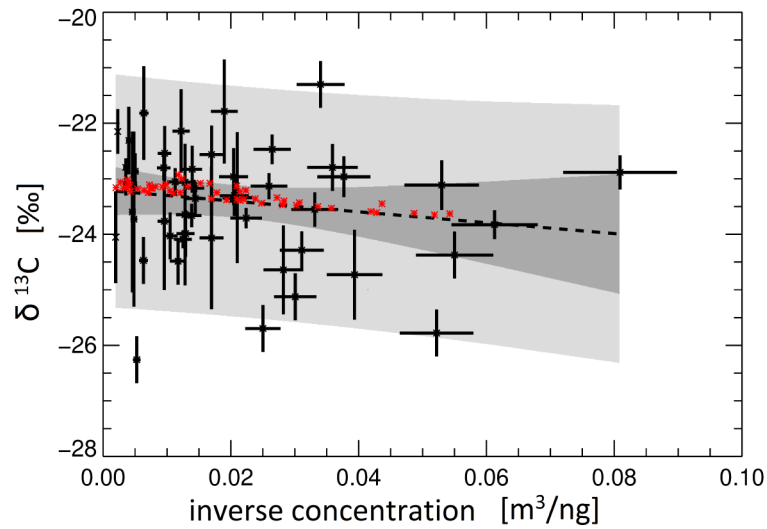


Figure 4.4.: Keeling plot of all LANUV measurements (black) and modeling (red). The linear fit of the measurements is black dashed, its 95 % confidence interval is marked dark grey. The area that contains with 95 % confidence all measurements is marked light grey. The model was initialized with initial and background δ -values derived from the y-intercept and tendency of the linear fit. The modeled data points are aged in a range of up to 0.25 ‰.

4. Case study

Isotopic signatures of source regions. Since the measured isotopic composition in the sampled aerosol is the one of sources, it is desirable to assign different source regions to individual isotopic signatures. For this study, the source regions were specified via the general direction the retroplume points to: North, North-West, West, South, East and Central. Central means that the plume is dispersed all over Central Europe. The aerosol source region for every retroplume is given in the 'info'-column of Appendix B. In Table 4.1, the weighted mean measured δ -value of every source region is given.

Table 4.1.: Isotopic signatures of source regions

Source region	$\delta^{13}\text{C}$ [‰]
North	-23.21 ± 0.07
North-West	-23.88 ± 0.04
West	-24.41 ± 0.03
South	-23.12 ± 0.05
East	-23.16 ± 0.07
Central	-23.39 ± 0.06

Aerosols from the West and North-West show a lower δ -value than the other source regions. This result confirms the interpretation of different sources having different $\delta^{13}\text{C}$. The isotopic signatures of the other source regions are very similar within measurement precision. Even if the retroplume points to one general wind direction, different source regions are generally inter-mixed. To gain significance also for other source regions, more measurements are necessary.

5. Conclusion and future research

Biomass burning aerosol is an important research topic due to its effects on air quality, climate and human health. Combining Lagrangian particle dispersion modeling with concentration- and isotopic measurements is an innovative tool for source apportionment of organic aerosol and investigations on its chemical and depositional loss.

This work shows that the implementation of two isotope tracers in the LPDM FLEXPART, ^{12}C -Levoglucosan and ^{13}C -Levoglucosan, to calculate the isotopic ratio distribution of the biomass burning tracer, was successful. The use of the full dispersed output, in combination with emission inventories via the 'folded retroplume technique' yields a very detailed information on the source–receptor relationships, allowing for quantifying source contributions and loss processes at the receptor and for supporting the interpretation of ambient measurements.

Sensitivity studies show that some model variables do not have a significant impact for this study. Excepting ca. 15 % of the days, the use of different meteorologies did not influence the modeling results above the error range. Chemical aging is no major influence during winter time, being below detection limit according to the model. Furthermore dry deposition is an insignificant process for fresh coalgulation mode biomass burning aerosol.

On the other hand, the use of the deposition module results in considerable reductions in the modelled concentration at the sampling site, depending of the time frame and intensity of the precipitations.

The present case study mostly shows good agreement between modeled and observed concentration data. While the model overestimates in few cases the levoglucosan concentration at the rural site, for the urban station the results diverge in both directions. This might be an indication for unrevealed precipitation events for the former and unidentified or poorly described source for the latter. As for the isotopic ratio modelling, the modeled δ -values do by far not show the variability of the measured ones. This is the result of unknown initial isotopic composition of individual sources. It is noticeable here that the simulated isotopic ratios vs. the inverse concentration are mostly situated on the line fitted to the measurements. Nevertheless, sensitivity and case study show in unison that local domestic heating sources are mostly contributing to the biomass burning aerosol burden in the investigated time frame.

This work demonstrates that the developed modeling strategies are a suitable method to assess sources of biomass burning aerosol in living areas in winter. The results indicate that the local emission mitigation is required. The sensitivity studies pointed out uncertainties for single

5. Conclusion and future research

processes, the comparison between simulated and observed isotopic ratios and concentration revealed the most probable sources and losses of the investigated aerosol.

In future research, more isotopic measurements of the fuels used for domestic heating in Europe should be carried out. Additional measurements can constrain isotopic signatures of individual sources. Global modeling and complementing measurement can provide information on concentration and isotopic composition of background aerosol. To assess chemical aging in a study, a biomass burning event with a homogeneous source in a radical-rich atmosphere should be chosen. Furthermore the influence of wet deposition should be included in all runs and also for isotope modeling. The developed strategies can be customized to different situations. When a careful assessment of all processes in sensitivity studies is carried out, the developed strategy is applicable to all kinds of emission and pollution scenarios.

A. Fortran/IDL code

Both used versions of FLEXPART (Version 9.0 and Version 10.2 beta) are modified to write formatted output files, in contrast to the original version that delivers unformatted sparse output files (based on Zhang [2015]). The modified routines are *concooutput.f90* and *writeheader.f90*.

The following IDL (Interactive Data Language) routines organize the input data, produce input files and redirect the output of FLEXPART to the save directories: *writeavailable.pro*, *writescript.pro*, *writecommand.pro*, *writereceptors.pro*, *writereleases.pro*.

The routines *postpipeline.pro*, *postread.pro*, *postconvert.pro* and *postloop.pro* process the FLEXPART model output. Hereof, *postread.pro* and *postconvert.pro* are adapted from Zhang [2015] with minor modifications. The output is then given as gridded retroplumes.

Furthermore, the routines *plotplumebg.pro*, *plotfoldbacklg.pro*, *plotpbl.pro* and *plotplumetimesteps.pro* fold and plot retroplumes, provide an overview of the mixing height and examine single time steps. The routine *plotpbl.pro* is provided by Dr. Iulia Gensch.

If not otherwise noted, the routines are self-written. All used program code, including the modified FLEXPART files, are stored on the enclosed CD-ROM.

B. Tabular results

This Appendix contains tables with measurement and modeling results: Overview of STYR and EIFEL runs, followed by the comparison of ECMWF and GFS meteorological input data and after hour heating.

The overview columns are marked as follows:

Date: Sampling date

δ exp: Measured δ -value of the sampled levoglucosan [‰]

c exp: Measured concentration of the sampled levoglucosan [ng/m^3]

δ mod: Modeled δ -value [‰]

c mod: Modeled concentration [ng/m^3]

backgr mod: Percentage of the modeled background [%]

emis mod: Percentage of the modeled emissions [%]

emis mod day 1 / 2 / 3 / r: Percentages of emissions that are 1-3 days old, and the rest [%]

Plume: Retroplumes in the footprint layer (blue) and in the full column (grey) for overview, on a logarithmic color scale [s] (see Figure B.1 for color code)

Folded plume: Retroplume in the footprint layer, folded with emission inventories, on a logarithmic color scale [ng/m^3] (see Figure B.1 for color code)

Emission contribution: Emissions that are 1-3 days old (red, yellow, blue), and the rest (grey)

Info: Overall wind direction, Source regions for emissions and background, information on sources, sinks and precipitation

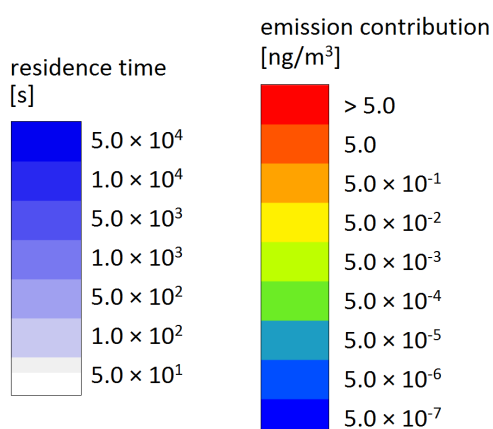

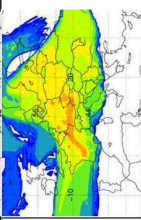
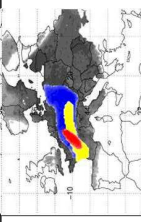

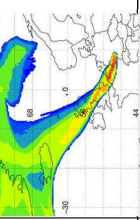
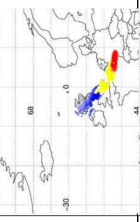

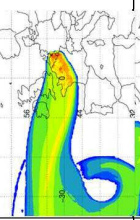
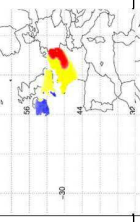
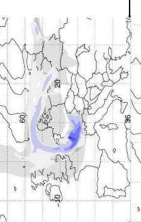
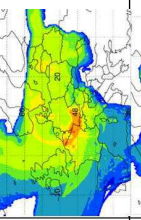
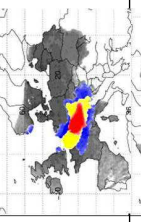

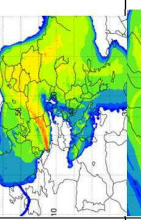
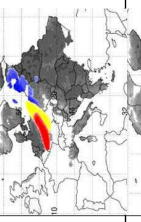

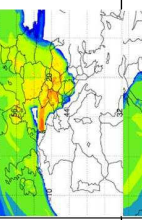
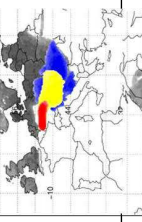
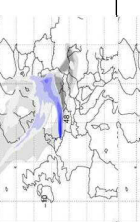
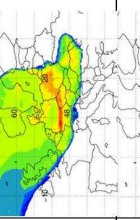
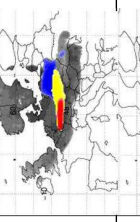
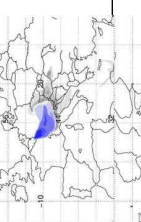
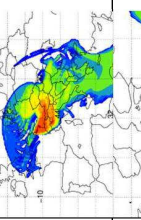
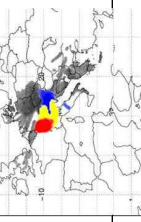
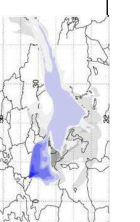
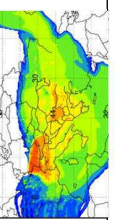
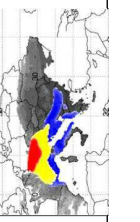


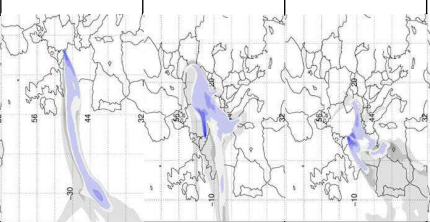
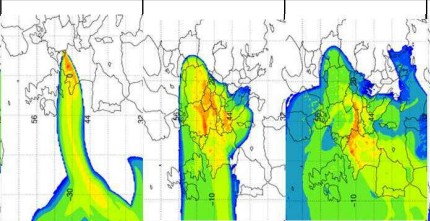
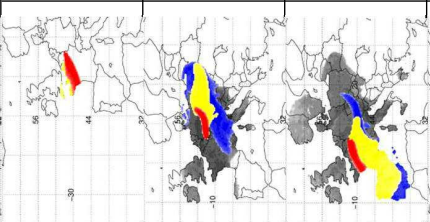
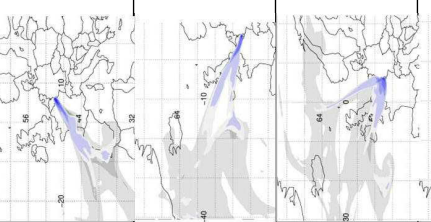
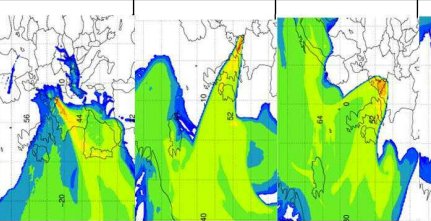
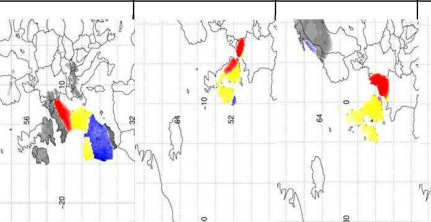
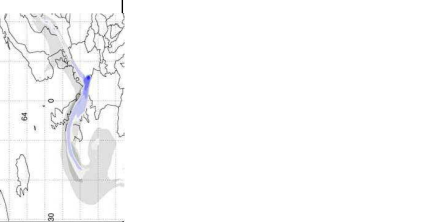
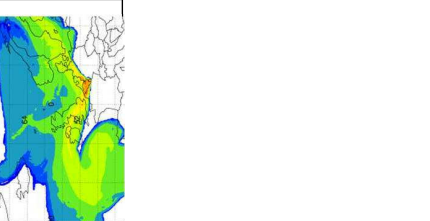
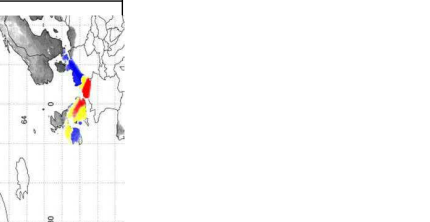



Figure B.1.: Color code for retroplumes (left) and folded retroplumes (right). Logarithmic scaling.

Overview EIFE

1/3

Number	Date	$\delta \text{ exp}$ [%]	$c \text{ exp}$ [ng/m ³]	$\delta \text{ mod}$ [%]	$c \text{ mod}$ [ng/m ³]	backgr mod [%]	emis mod [%]	emis mod day1 / 2 / 3 / r [%]	Plume <small>(footprint layer, Hintergrund)</small>	Folded plume (incl. background)	Emission contribution $d1, d2, d3, r$	Info
1	02.11.2015	-23,70 ± 0,18	44,66 ± 4,91	-23,02	263,03	4,71	95,29	16,0 / 56,1 / 23,9 / 3,84				<ul style="list-style-type: none"> - Sources: South-west Germany, Switzerland, Northern Italy, Vosges (France), Austria). - Background: Southern Europe, Mediterranean Sea. - Model overestimates concentration - unknown loss. Rainy in the south.
2	06.11.2015	-21,30 ± 0,42	29,39 ± 3,23	-23,34	36,75	33,74	66,26	37,7 / 41,8 / 16,1 / 4,30				<ul style="list-style-type: none"> - Sources: West, Luxemburg, Southern Belgium, Central France. - Background: South-west Europe, Mediterranean Sea, Atlantic Ocean. - Light rain in the north
3	10.11.2015	-22,89 ± 0,31	12,36 ± 1,36	-23,26	90,88	13,64	86,36	74,2 / 25,7 / 0,00 / 0,00				<ul style="list-style-type: none"> - Sources: West, Luxemburg, Southern Belgium, Southern France. - Background: Atlantic Ocean, northern part. - Model overestimates concentration - unknown loss. - Precipitation in the direction of the retroplume.
4	14.11.2015	-22,96 ± 0,37	26,54 ± 2,92	-23,50	29,75	41,68	58,32	83,1 / 16,8 / 0,00 / 0,00				<ul style="list-style-type: none"> - Sources: West, Luxemburg, Southern Belgium, Southern France. - Background: Atlantic Ocean, northern part. - Light precipitation.
5	22.11.2015	-24,64 ± 0,80	35,43 ± 3,90	-23,59	23,85	52,00	48,00	64,8 / 26,2 / 5,92 / 3,02				<ul style="list-style-type: none"> - Sources: North, Benelux, (GB), (Northern Germany), (Scandinavia). - Background: North Sea, Norwegian Sea. - Precipitation.
6	26.11.2015	-23,1317 ± 0,23	38,51 ± 4,24	-23,48	33,04	37,53	62,47	70,2 / 29,7 / 0,00 / 0,00				<ul style="list-style-type: none"> - Sources: North, Benelux, (Northern GB). - Background: Norwegian Sea, incl. Iceland and Greenland. - Light precipitation.
7	08.12.2015	-23,17 ± 0,15	70,23 ± 7,73	-23,17	130,20	9,52	90,48	25,0 / 51,4 / 15,3 / 8,16				<ul style="list-style-type: none"> - Sources: West, Luxemburg, France, (Spain), (Italy). - Background: Mediterranean Sea, Atlantic Ocean. - Precipitation.
8	10.02.2016	-24,37 ± 0,42	18,18 ± 2,00	-23,53	27,98	44,32	55,68	66,9 / 31,1 / 0,01 / 1,85				<ul style="list-style-type: none"> - Sources: West, (North-West), Luxemburg, Northern France, GB, (Scandinavia). - Background: Norwegian Sea, Atlantic Ocean (Iceland, Greenland). - Precipitation.
9	14.02.2016	-23,65 ± 1,27	78,00 ± 8,58	-23,14	122,10	10,16	89,84	22,6 / 57,0 / 15,4 / 4,81				<ul style="list-style-type: none"> - Sources: Central, Central Europe. - Background: Atlantic Ocean, (Norwegian Sea). - Occasional precipitation.


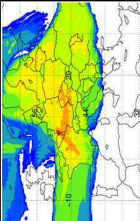
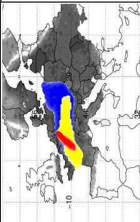

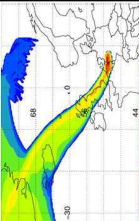
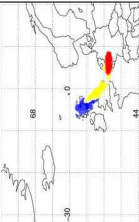
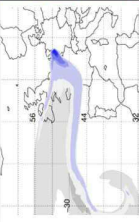
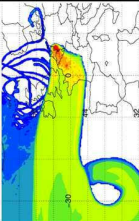
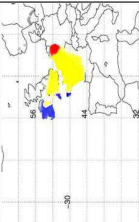
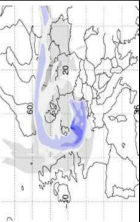
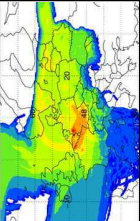
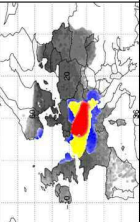
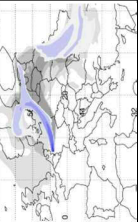
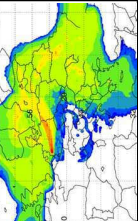
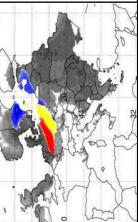
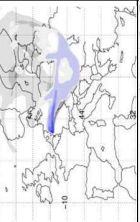
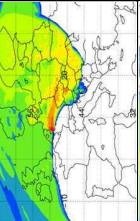
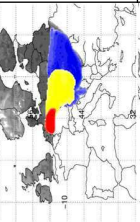
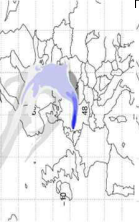
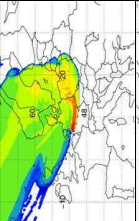
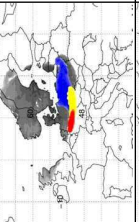
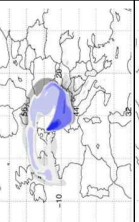
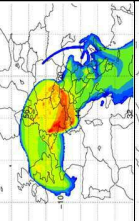
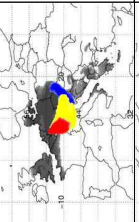
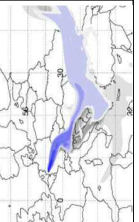
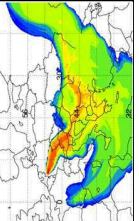
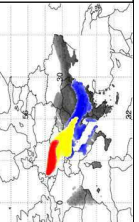
10	18.02.2016	-22,804 ± 0,22	105,35 ± 11,59	-23,00	81,30	15,25	84,75	10,7 / 21,1 / 22,4 / 45,7				<ul style="list-style-type: none"> - Sources: Central, (West), Central Europe. - Background: Atlantic Ocean, Baltic Sea, (Norwegian Sea). - Very few precipitation.
11	26.02.2016	-23,962 ± 0,42	77,5 ± 8,53	-23,36	42,01	29,52	70,48	33,6 / 60,8 / 5,41 / 0,08				<ul style="list-style-type: none"> - Sources: North-West, Western Germany, Belgium, Luxembourg, northern France, GB. - Background: Norwegian Sea, (Iceland), (Greenland). - No precipitation in the direction of the retroplume.
12	05.03.2016	-25,70 ± 0,42	39,99 ± 4,40	-23,23	46,76	26,52	73,48	31,1 / 67,8 / 1,05 / 0,00				<ul style="list-style-type: none"> - Sources: West, (North-West), Western Germany, Benelux, GB. - Background: Atlantic Ocean. - Precipitation.
13	09.03.2016	-24,06 ± 1,28	58,93 ± 6,48	-23,08	59,87	20,71	79,29	41,8 / 26,0 / 15,8 / 16,1				<ul style="list-style-type: none"> - Sources: Central, (West), Central Europe, mainly Southern Germany, Austria, Luxembourg, north-east France. - Background: Full Europe, Mediterranean Sea, Atlantic Ocean, Norwegian Sea, Baltic Sea. - Light precipitation in the direction of the retroplume.
14	13.03.2016	-22,96 ± 0,51	48,97 ± 5,39	-23,21	44,77	27,70	72,30	37,8 / 35,1 / 6,08 / 20,9				<ul style="list-style-type: none"> - Sources: Central, (East), Central German, Poland, Baltic States, (Eastern Europe). - Background: Norwegian Sea, Mediterranean Sea, Baltic Sea. - Light precipitation in the direction of the retroplume.
15	17.03.2016	-23,06 ± 0,25	88,65 ± 9,75	-23,08	65,72	18,87	81,13	34,2 / 38,5 / 10,6 / 16,6				<ul style="list-style-type: none"> - Sources: East, Central Germany, Switzerland, Czech Republic, Southeast Europe, (northern Europe). - Background: Norwegian Sea. - No precipitation.
16	19.01.2017	-23,76 ± 1,24	104,41 ± 11,49	-23,21	156,03	7,95	92,05	48,8 / 35,2 / 4,90 / 11,0				<ul style="list-style-type: none"> - Sources: East, Central Germany, Czech Republic, Poland. - Background: Baltic Sea, Norwegian Sea. - No precipitation in the direction of the retroplume.
17	27.01.2017	-22,54 ± 0,49	103,90 ± 11,43	-23,16	277,61	4,47	95,53	33,0 / 48,8 / 12,6 / 5,47				<ul style="list-style-type: none"> - Sources: South, Southern Germany, Western France, Austria, Switzerland, Northern Italy, (Europe). - Background: Mediterranean Sea, North Sea, Africa. - Model overestimates concentration - unknown loss. - Heavy rain in source regions.
18	12.02.2017	-21,82 ± 0,84	156,74 ± 17,24	-23,06	251,87	4,92	95,08	29,8 / 53,3 / 7,45 / 9,29				<ul style="list-style-type: none"> - Sources: South, Southern Germany, Austria, Switzerland, Western France, Northern Italy, (Southeast Europe). - Background: Mediterranean Sea. - Model overestimates concentration - unknown loss. - Light precipitation.

19	20.03.2017	-25,78 ± 0,42	19,16 ± 2,11	-23,43	32,55	38,10	61,90	74,2 / 25,7 / 0,00 / 0,00				<ul style="list-style-type: none"> - Sources: West, (North-West), Luxembourg, Southern Belgium, Northern France. - Background: Atlantic Ocean. - Heavy precipitation.
20	24.03.2017	-23,66 ± 0,21	72,16 ± 7,94	-22,93	84,93	14,60	85,40	24,3 / 31,0 / 17,2 / 27,4				<ul style="list-style-type: none"> - Sources: East, Central Germany, Czech Republic, Poland, Central Europe. - Background: Atlantic Ocean. - Precipitation in source regions.
21	28.03.2017	-22,80 ± 0,42	27,86 ± 3,06	-23,13	47,79	25,95	74,05	39,7 / 31,8 / 18,3 / 10,0				<ul style="list-style-type: none"> - Sources: South, (West), South-west Germany, Austria, Northern Italy, France, Luxembourg, (Spain). - Background: Mediterranean Sea, North Sea, Atlantic Ocean, Baltic Sea. - Very few precipitation.
22	01.04.2017	-24,29 ± 0,34	32,16 ± 3,54	-23,58	19,75	62,78	37,22	50,5 / 38,2 / 7,32 / 3,82				<ul style="list-style-type: none"> - Sources: West, Luxembourg, Southern Belgium, Central France, (Spain), (GB). - Background: Atlantic Ocean. - Precipitation on sampling day.
23	13.04.2017	-23,83 ± 0,26	16,32 ± 1,80	-23,65	19,28	64,31	35,69	63,9 / 35,9 / 0,07 / 0,00				<ul style="list-style-type: none"> - Sources: North-West, Luxembourg, Belgium, GB. - Background: Northern Atlantic, (Iceland), (Greenland). - Precipitation on sampling day.
24	17.04.2017	-23,11 ± 0,45	18,87 ± 2,08	-23,62	20,54	60,38	39,62	55,8 / 43,9 / 0,12 / 0,13				<ul style="list-style-type: none"> - Sources: North-West, Northern France, Luxembourg, Belgium, Netherlands, Western Germany, (GB). - Background: North Sea, Norwegian Sea, Atlantic Ocean, (Iceland). - Precipitation on sampling day.
25	21.04.2017	-23,55 ± 0,31	30,19 ± 3,32	-23,45	22,91	54,12	45,88	32,4 / 49,7 / 13,6 / 4,22				<ul style="list-style-type: none"> - Sources: North-West, Northern France, Luxembourg, Belgium, Netherlands, Northern Germany, (GB), (Scandinavia). - Background: North Sea, Norwegian Sea, Atlantic Ocean, Baltic Sea. - Very few precipitation in the direction of the retroplume.

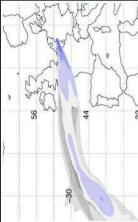
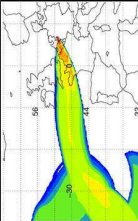
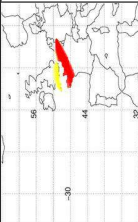
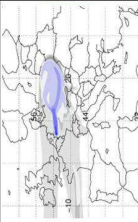
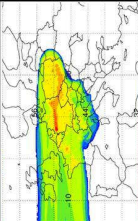
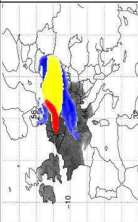
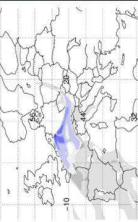
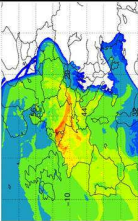
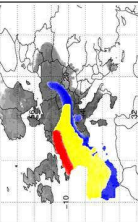
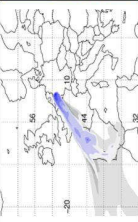
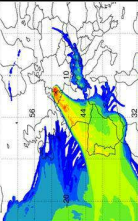
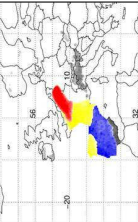
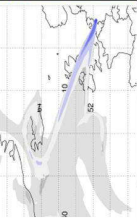
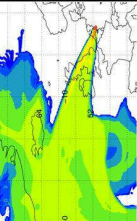
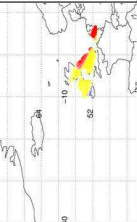
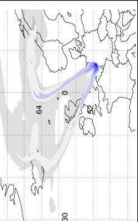
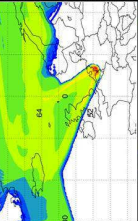
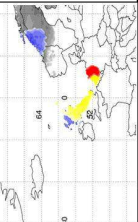
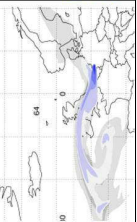
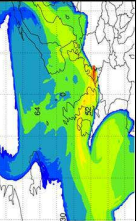
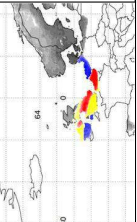
Overview STYR 1/3

Number	Date	$\delta \text{ exp}$ [%]	$c \text{ exp}$ [ng/m ³]	$\delta \text{ mod}$ [%]	$c \text{ mod}$ [ng/m ³]	backgr mod [%]	emis mod [%]	emis mod day1 / 2 / 3 / r [%]	Plume <small>(footprint layer, hinterground)</small>	Folded plume (incl. background)	Emission contribution(d1, d2, d3, r)	Info
1	02.11.2015	-24,05 ± 0,83	509,48 ± 56,04	-23,06	370,91	3,34	96,66	33,5 / 42,2 / 20,7 / 3,44				- Sources: South, South-West Germany, Austria, Switzerland, Northern Italy, Slovenia, (South Europe) - Background: South Europe, Mediterranean Sea - Rainy in the south. Model overestimates concentration.
2	06.11.2015	-22,56 ± 0,52	58,91 ± 6,48	-23,25	82,95	14,95	85,05	76,7 / 16,2 / 5,34 / 1,66				- Sources: West, Limburg, Belgium, Luxembourg, France, Spain, Portugal (South-West Europe) - Background: Atlantic Ocean, Mediterranean Sea, South-West Europe, (Africa) - Light rain in the north.
3	10.11.2015	-25,12 ± 0,42	33,25 ± 3,66	-23,39	46,65	26,58	73,42	88,7 / 11,2 / 0,00 / 0,00				- Sources: West, South Netherlands, Belgium, North of France, (Southern UK). - Background: Atlantic Ocean, (Northern Atlantic Ocean). - Precipitation in the direction of the retroplume.
4	14.11.2015	-23,34 ± 1,18	47,61 ± 5,24	-23,47	35,58	34,85	65,15	96,4 / 3,52 / 0,00 / 0,00				- Sources: West, South Netherlands, Belgium, North of France, (Southern UK). - Background: Atlantic Ocean, (Northern Atlantic Ocean). - Light precipitation.
5	22.11.2015	-22,88 ± 0,42	71,70 ± 7,89	-23,44	40,32	30,75	69,25	91,9 / 6,38 / 1,03 / 0,67				- Sources: North, Netherlands, Scandinavia, (Northern Europe). - Background: Northern Europe including Oceans. - Precipitation.
6	26.11.2015	-23,11 ± 0,18	208,13 ± 22,89	-23,36	58,97	21,03	78,97	92,9 / 7,01 / 0,00 / 0,00				- Sources: North, Southern Belgium, Netherlands, (Northern UK), (Iceland?). - Background: Norwegian Sea including Iceland and Greenland. - Light precipitation. Measurements strongly influenced by local sources.
7	08.12.2015	-22,14 ± 0,75	81,91 ± 9,01	-23,18	185,26	6,69	93,31	43,4 / 39,4 / 12,5 / 4,60				- Sources: West, Western Germany, Limburg, Belgium, France, Northern Italy, Spain, Portugal. - Background: Mediterranean Sea, Southern Atlantic Ocean, (Africa). - Precipitation.
8	10.02.2016	-21,79 ± 0,94	52,71 ± 5,80	-23,38	51,72	23,98	76,02	83,5 / 14,4 / 0,11 / 1,89				- Sources: West, (North-West), Netherlands, Belgium, Southern France, UK, (France), (Scandinavia). - Background: Northwest Europe, Norwegian Sea, Atlantic Ocean, (Iceland, Greenland). - Precipitation.
9	14.02.2016	-23,73 ± 1,58	207,06 ± 22,78	-23,17	310,57	3,99	96,01	65,8 / 25,6 / 6,51 / 2,00				- Sources: Central, Mainly Germany, Poland, Czech Republic, Switzerland, Austria, Northern Italy, France, (Central to Eastern Europe). - Background: Atlantic Ocean, (Norwegian Sea), Mediterranean Sea. - Occasional precipitation. Model overestimates concentration.

Overview STYR 2/3

10	18.02.2016	-22,87 ± 0,32	199,39 ± 21,93	-23,11	137,99	8,99	91,01	48,0 / 19,8 / 10,6 / 21,5	  	- Sources: Central, (West). Germany, Czech Republic, Switzerland, Central France, (Europe). - Background: Baltic Sea, Atlantic Ocean, (Norwegian Sea), (Mediterranean Sea). - Very few precipitation.
11	26.02.2016	-26,26 ± 0,42	189,86 ± 20,88	-23,25	141,31	8,78	91,22	77,5 / 21,9 / 0,49 / 0,00	  	- Sources: North-West Southern Netherlands, Belgium, UK. - Background: Direction Greenland and Iceland. - No precipitation in the direction of the retroplume.
12	05.03.2016	-22,80 ± 0,16	282,26 ± 31,05	-23,14	252,47	4,91	95,09	60,8 / 38,5 / 0,54 / 8,69	  	- Sources: West, (North-West). Netherlands, Belgium, Northern France, (Southern UK). - Background: Atlantic Ocean. - Precipitation.
13	09.03.2016	-24,02 ± 0,42	95,21 ± 10,47	-23,10	101,94	12,16	87,84	60,0 / 21,5 / 5,83 / 12,5	  	- Sources: Central, (West). Central Germany, Belgium, South-East France, (Europe). - Background: Norwegian Sea, (Atlantic Ocean), (Mediterranean Sea). - Light precipitation in the direction of the retroplume.
14	13.03.2016	-24,48 ± 0,42	85,26 ± 9,38	-23,22	95,66	12,96	87,04	77,2 / 15,4 / 0,74 / 6,53	  	- Sources: Central, (East). Central Germany, Poland, (North-West Europe). - Background: Baltic Sea, Norwegian Sea, (Mediterranean Sea). - Light precipitation in the direction of the retroplume.
15	17.03.2016	-23,60 ± 1,45	217,82 ± 23,96	-23,17	134,00	9,25	90,75	73,1 / 18,0 / 3,53 / 5,32	  	- Sources: East. Central Germany, Switzerland, Czech Republic, Poland, Eastern Europe, (Scandinavia). - Background: Baltic Sea, Norwegian Sea, (Atlantic Ocean). - No precipitation. Measurements strongly influenced by local sources.
16	19.01.2017	-22,15 ± 0,40	434,85 ± 47,83	-23,23	232,70	5,33	94,67	72,5 / 22,0 / 3,13 / 2,17	  	- Sources: East. Central Germany, Poland, Southern Czech Republic, Baltic States, Scandinavia. - Background: Baltic Sea, Norwegian Sea. - No precipitation in the direction of the retroplume. Measurements strongly influenced by local sources.
17	27.01.2017	-23,10 ± 0,20	281,86 ± 31,00	-23,16	494,91	2,51	97,49	46,2 / 36,8 / 12,3 / 4,57	  	- Sources: South, Southern Germany, Czech Republic, Switzerland, Northern Italy, Austria, (Whole Europe). - Background: (North Sea), (Mediterranean Sea). - Heavy rain in source regions. Model overestimates concentration.
18	12.02.2017	-22,31 ± 0,61	248,32 ± 27,32	-23,11	240,47	5,16	94,84	46,8 / 25,4 / 16,9 / 10,7	  	- Sources: South, Central Germany, Czech Republic, Switzerland, Slovenia, Croatia, Hungary, (South-East Europe). - Background: Mediterranean Sea, (Africa), (Asia). - Light precipitation.

Overview STYR 3/3

19	20.03.2017	-24,47 ± 0,42	158,45 ± 17,43	-23,37	47,70	26,00	74,00	88,8 / 111,1 / 0,00 / 0,00	  	- Sources: West, (North-West), Southern Netherlands, Belgium, Southern UK, Northern France. - Background: Atlantic Ocean. - Heavy precipitation. Measurements strongly influenced by local sources.
20	24.03.2017	-23,06 ± 0,40	77,99 ± 8,58	-23,15	107,23	11,56	88,44	65,3 / 17,6 / 7,32 / 9,70	  	- Sources: East, Central Germany, Poland, Czech Republic, Central Europe. - Background: Atlantic Ocean, (Norwegian Sea), (Mediterranean Sea). - Precipitation in source regions.
21	28.03.2017	-23,30 ± 0,36	48,67 ± 5,35	-23,14	75,66	16,39	83,61	55,1 / 30,0 / 9,76 / 5,07	  	- Sources: South, (West), Southwest Germany, Limburg, Belgium, Northern France, Austria, Switzerland, South Europe, (Central Europe). - Background: All Oceans around Europe, (Africa). - Very few precipitation.
22	01.04.2017	-23,36 ± 0,30	69,28 ± 7,62	-23,25	56,19	22,07	77,93	59,1 / 38,7 / 1,41 / 0,68	  	- Sources: West, Limburg, Belgium, France, (Spain), (Portugal), (Northern Italy). - Background: Atlantic Ocean, (Mediterranean Sea). - Precipitation on sampling day.
23	13.04.2017	-24,73 ± 0,81	25,41 ± 2,80	-23,61	23,35	53,10	46,90	93,1 / 6,79 / 0,00 / 0,00	  	- Sources: North-West, Netherlands, Northern Belgium, UK. - Background: Northern Atlantic Ocean, (Iceland), (Greenland). - Precipitation on sampling day.
24	17.04.2017	-22,47 ± 0,27	37,79 ± 4,16	-23,37	45,37	27,33	72,67	79,2 / 20,6 / 0,00 / 0,06	  	- Sources: North-West, Netherlands, Northern Belgium, Northern UK, (Northern Scandinavia). - Background: Norwegian Sea. - Precipitation on sampling day.
25	21.04.2017	-24,08 ± 0,16	80,05 ± 8,81	-23,40	35,32	35,11	64,89	68,3 / 28,2 / 1,81 / 1,54	  	- Sources: North-West, Netherlands, Northern Belgium, UK, Northern France, Northern Germany, (Scandinavia). - Background: Atlantic Ocean, (Norwegian Sea), (Baltic Sea). - Very few precipitation in the direction of the retroplume.

Compare Meteorologies

ECMWF

GFAS

Differences

Date	EIFE			STYR			EIFE			STYR		
	δ mod [%]	c mod [ng/m ³]	δ mod [%]	δ mod [%]	c mod [ng/m ³]	δ mod [%]	δ mod [%]	c mod [ng/m ³]	δ mod [%]	δ mod [%]	c mod [ng/m ³]	c mod [ng/m ³]
02.11.2015	-23,02	263,03	-23,06	-23,04	370,91	212,58	-23,14	258,98	-23,14	-23,14	258,98	258,98
06.11.2015	-23,34	36,75	-23,25	-23,35	82,95	38,23	-23,30	67,06	-23,30	-23,30	67,06	67,06
10.11.2015	-23,26	90,88	-23,39	-23,27	46,65	80,60	-23,43	41,80	-23,43	-23,43	41,80	41,80
14.11.2015	-23,50	29,75	-23,47	-23,49	35,58	31,16	-23,49	33,53	-23,49	-23,49	33,53	33,53
22.11.2015	-23,59	23,85	-23,44	-23,61	40,32	23,19	-23,47	36,02	-23,47	-23,47	36,02	36,02
26.11.2015	-23,48	33,04	-23,36	-23,43	58,97	38,08	-23,34	66,96	-23,34	-23,34	66,96	66,96
08.12.2015	-23,17	130,20	-23,18	-23,21	185,26	76,09	-23,24	90,13	-23,24	-23,24	90,13	90,13
10.02.2016	-23,53	27,98	-23,38	-23,58	51,72	25,00	-23,41	45,77	-23,41	-23,41	45,77	45,77
14.02.2016	-23,14	122,10	-23,17	-23,12	310,57	128,76	-23,18	284,61	-23,18	-23,18	284,61	284,61
18.02.2016	-23,00	81,30	-23,11	-23,03	137,99	69,88	-23,11	148,15	-23,11	-23,11	148,15	148,15
26.02.2016	-23,36	42,01	-23,25	-23,36	141,31	44,07	-23,23	168,16	-23,23	-23,23	168,16	168,16
05.03.2016	-23,23	46,76	-23,14	-23,06	252,47	129,19	-23,21	191,58	-23,21	-23,21	191,58	191,58
09.03.2016	-23,08	59,87	-23,10	-23,11	101,94	57,79	-23,16	86,56	-23,16	-23,16	86,56	86,56
13.03.2016	-23,21	44,77	-23,22	-23,18	95,66	45,08	-23,23	89,16	-23,23	-23,23	89,16	89,16
17.03.2016	-23,08	65,72	-23,17	-23,06	134,00	72,25	-23,16	135,91	-23,16	-23,16	135,91	135,91
19.01.2017	-23,21	156,03	-23,23	-23,26	232,70	96,79	-23,23	275,36	-23,23	-23,23	275,36	275,36
27.01.2017	-23,16	277,61	-23,16	-23,18	494,91	200,45	-23,19	249,99	-23,19	-23,19	249,99	249,99
12.02.2017	-23,06	251,87	-23,11	-23,10	240,47	153,43	-23,10	222,51	-23,10	-23,10	222,51	222,51
20.03.2017	-23,43	32,55	-23,37	-23,46	47,70	29,22	-23,35	50,63	-23,35	-23,35	50,63	50,63
24.03.2017	-22,93	84,93	-23,15	-23,23	107,23	42,25	-23,18	99,96	-23,18	-23,18	99,96	99,96
28.03.2017	-23,13	47,79	-23,14	-23,08	75,66	54,61	-23,09	91,77	-23,09	-23,09	91,77	91,77
01.04.2017	-23,63	18,43	-23,25	-23,41	56,19	27,13	-23,19	73,49	-23,19	-23,19	73,49	73,49
13.04.2017	-23,65	19,28	-23,61	-23,74	23,35	17,00	-23,58	24,82	-23,58	-23,58	24,82	24,82
17.04.2017	-23,62	20,54	-23,37	-23,58	45,37	22,30	-23,36	51,14	-23,36	-23,36	51,14	51,14
21.04.2017	-23,45	22,91	-23,40	-23,48	35,32	22,99	-23,39	36,74	-23,39	-23,39	36,74	36,74

	EIFE			STYR		
	δ mod (abs) [%]	c mod (rel) [%]	δ mod (abs) [%]	δ mod (rel) [%]	c mod (rel) [%]	c mod (rel) [%]
	0,02	19,18	0,07	30,18	30,18	30,18
	0,01	-4,00	0,05	19,16	19,16	19,16
	0,01	11,31	0,03	10,39	10,39	10,39
	-0,01	-4,73	0,02	5,75	5,75	5,75
	0,02	2,76	0,03	10,68	10,68	10,68
	-0,05	-15,27	-0,02	-13,55	-13,55	-13,55
	0,04	41,56	0,05	51,35	51,35	51,35
	0,05	10,65	0,03	11,51	11,51	11,51
	-0,02	-5,46	0,01	8,36	8,36	8,36
	0,03	14,05	0,00	-7,37	-7,37	-7,37
	0,00	-4,91	-0,01	-19,00	-19,00	-19,00
	-0,17	-176,29	0,06	24,12	24,12	24,12
	0,02	3,46	0,06	15,09	15,09	15,09
	-0,03	-0,69	0,00	6,80	6,80	6,80
	-0,02	-9,93	-0,01	-1,43	-1,43	-1,43
	0,05	37,97	0,01	-18,33	-18,33	-18,33
	0,02	27,80	0,03	49,49	49,49	49,49
	0,04	39,08	-0,02	7,47	7,47	7,47
	0,03	10,21	-0,02	-6,15	-6,15	-6,15
	0,30	50,26	0,03	6,78	6,78	6,78
	-0,05	-14,27	-0,05	-21,30	-21,30	-21,30
	-0,22	-47,18	-0,06	-30,79	-30,79	-30,79
	0,09	11,81	-0,02	-6,26	-6,26	-6,26
	-0,04	-8,57	-0,01	-12,72	-12,72	-12,72
	0,03	-0,35	-0,01	-4,04	-4,04	-4,04
Mean	0,01	-0,46	0,01	4,65	4,65	4,65
Std	0,09	41,51	0,03	19,83	19,83	19,83

After hour heating

EIFEL station	c mod [ng/m ³]	c mod 5pm-11pm [ng/m ³]	deviation [%]
02.11.2015	263,03	252,70	3,93
06.11.2015	36,75	35,16	4,34
10.11.2015	90,88	75,92	16,47
14.11.2015	29,75	22,65	23,86
22.11.2015	23,85	24,04	-0,81
26.11.2015	33,04	32,10	2,84
08.12.2015	130,20	143,35	-10,10
10.02.2016	27,98	30,17	-7,81
14.02.2016	122,10	150,87	-23,56
18.02.2016	81,30	81,77	-0,58
26.02.2016	42,01	40,37	3,89
05.03.2016	46,76	45,95	1,74
09.03.2016	59,87	53,03	11,41
13.03.2016	44,77	46,70	-4,31
17.03.2016	65,72	57,57	12,40
19.01.2017	156,03	171,00	-9,59
27.01.2017	277,61	278,04	-0,15
12.02.2017	251,87	244,71	2,84
20.03.2017	32,55	27,93	14,18
24.03.2017	84,93	99,63	-17,30
28.03.2017	47,79	50,27	-5,20
01.04.2017	18,43	18,79	-1,97
13.04.2017	19,28	20,40	-5,77
17.04.2017	20,54	23,35	-13,69
21.04.2017	22,91	23,19	-1,23
			Mean -0,17
			Std 10,54

B. Tabular results

Bibliography

- Markus Amann, Janusz Cofala, Zbigniew Klimont, Christian Nagel, and Wolfgang Schieder. Measures to address air pollution from small combustion sources. Umweltbundesamt, 2018.
- W. M. Angevine, J. Brioude, S. McKeen, and J. S. Holloway. Uncertainty in Lagrangian pollutant transport simulations due to meteorological uncertainty from a mesoscale WRF ensemble. *Geoscientific Model Development*, 7(6):2817–2829, 2014.
- G. Baumbach, M. Struschka, W. Juschka, M. Carrasco, K. B. Ang, L. Hu, W. Bächlin, and C. Sörgel. Modellrechnungen zu den Immissionsbelastungen bei einer verstärkten Verfeuerung von Biomasse in Feuerungsanlagen der 1. BImSchV. UBA-FB 001355, Umweltbundesamt, 2010.
- Isabelle Bey, Daniel J. Jacob, Jennifer. A. Logan, and Robert M. Yantosca. Asian chemical outflow to the pacific in spring: Origins, pathways, and budgets. *Journal of Geophysical Research: Atmospheres*, 106(D19):23097–23113, 2001. ISSN 2156-2202.
- J. Cozic, B. Verheggen, S. Mertes, P. Connolly, K. Bower, A. Petzold, U. Baltensperger, and E. Weingartner. Scavenging of black carbon in mixed phase clouds at the high alpine site Jungfraujoch. *Atmospheric Chemistry and Physics*, 7(7):1797–1807, 2007.
- Harmon Craig. Isotopic standards for carbon and oxygen and correction factors for mass-spectrometric analysis of carbon dioxide. *Geochimica et Cosmochimica Acta*, 12:133–149, 1957.
- Brittany D. Busby, Tony J. Ward, Jay R. Turner, and Christopher Palmer. Comparison and evaluation of methods to apportion ambient PM_{2.5} to residential wood heating in Fairbanks, AK. *Aerosol and Air Quality Research*, 2015.
- L. S. Davis and H. F. Dacre. Can dispersion model predictions be improved by increasing the temporal and spatial resolution of the meteorological input data? *Weather*, 64:232 – 237, 09 2009.
- Przemko Döring, Sebastian Glasenapp, and Udo Mantau. Rohstoffmonitoring Holz: Energieholzverwendung in privaten Haushalten 2014, Marktvolumen und verwendete Holzsortimente. Universität Hamburg, Zentrum Holzwirtschaft, 2016.
- S. Eckhardt, M. Cassiani, N. Evangeliou, E. Sollum, I. Pisso, and A. Stohl. Source–receptor matrix calculation for deposited mass with the Lagrangian particle dispersion model FLEXPART v10.2 in backward mode. *Geoscientific Model Development*, 10(12):4605–4618, 2017.

Bibliography

- Kerry A. Emanuel and Marina Živković Rothman. Development and evaluation of a convection scheme for use in climate models. *Journal of the Atmospheric Sciences*, 56(11):1766–1782, 1999.
- Philip M. Fine, Glen R. Cass, and Bernd R. T. Simoneit. Chemical Characterization of Fine Particle Emissions from the Fireplace Combustion of Woods Grown in the Southern United States. *Environmental Science & Technology*, 2002.
- Philip M. Fine, Glen R. Cass, and Bernd R.T. Simoneit. Chemical characterization of fine particle emissions from the wood stove combustion of prevalent united states tree species. *Environmental Engineering Science*, 21(6):705–721, 2004.
- I. Gensch, X.F. Sang, W. Laumer, C.Y. Chan, G. Engling, and A. Kiendler-Scharr. Using $\delta^{13}\text{C}$ of levoglucosan as a chemical clock. *Environmental Science and Technology*, 2018.
- Iulia Gensch, Werner Laumer, Olaf Stein, Beatrix Kammer, Thorsten Hohaus, Harald Saathoff, Robert Wegener, Andreas Wahner, and Astrid Kiendler-Scharr. Temperature dependence of the kinetic isotope effect in β -pinene ozonolysis. *Journal of Geophysical Research: Atmospheres*, 116(D20), 2011.
- H. Grythe, N. I. Kristiansen, C. D. Groot Zwaafink, S. Eckhardt, J. Ström, P. Tunved, R. Krejci, and A. Stohl. A new aerosol wet removal scheme for the Lagrangian particle model FLEXPART v10. *Geoscientific Model Development*, 10(4):1447–1466, 2017.
- M. Hallquist, J. C. Wenger, U. Baltensperger, Y. Rudich, D. Simpson, M. Claeys, J. Dommen, N. M. Donahue, C. George, A. H. Goldstein, J. F. Hamilton, H. Herrmann, T. Hoffmann, Y. Iinuma, M. Jang, M. E. Jenkin, J. L. Jimenez, A. Kiendler-Scharr, W. Maenhaut, G. McFiggans, Th. F. Mentel, A. Monod, A. S. H. Prévôt, J. H. Seinfeld, J. D. Surratt, R. Szmigielski, and J. Wildt. The formation, properties and impact of secondary organic aerosol: current and emerging issues. *Atmospheric Chemistry and Physics*, 9(14):5155–5236, 2009.
- Christopher J. Hennigan, Amy P. Sullivan, Jeffrey L. Collett Jr., and Allen L. Robinson. Levoglucosan stability in biomass burning particles exposed to hydroxyl radicals. *Geophysical Research Letters*, 37(9), 2010.
- I. Hüser, H. Harder, A. Heil, and J. W. Kaiser. Assumptions about footprint layer heights influence the quantification of emission sources: a case study for Cyprus. *Atmospheric Chemistry and Physics*, 17(18):10955–10967, 2017.
- Jorge Jimenez, Oscar Farias, Roberto Quiroz, and Jorge Yañez. Emission factors of particulate matter, polycyclic aromatic hydrocarbons, and levoglucosan from wood combustion in south-central Chile. *Journal of the Air & Waste Management Association*, 67(7):806–813, 2017.

- J. C. Lin. *Lagrangian Modeling of the Atmosphere*, chapter An Introduction, pages 2–3. American Geophysical Union, Washington, D. C., 2013.
- R. C. Owen and R. E. Honrath. Technical note: a new method for the Lagrangian tracking of pollution plumes from source to receptor using gridded model output. *Atmospheric Chemistry and Physics*, 9(7):2577–2595, 2009.
- S. Petterssen. *Weather Analysis and Forecasting*, pages 221–223. McGraw-Hill Book Company, New York, 1940.
- Jeffrey Reid, P V. Hobbs, Ronald Ferek, D R. Blake, J Vanderlei Martins, M R. Dunlap, and C Liousse. Physical, chemical, and optical properties of regional hazes dominated by smoke in Brazil. *JOURNAL OF GEOPHYSICAL RESEARCH-ATMOSPHERES*, 103:32059–32080, 12 1998.
- J. Rudolph and E. Czuba. On the use of isotopic composition measurements of volatile organic compounds to determine the "photochemical age" of an air mass. *Geophysical Research Letters*, 27(23):3865–3868, 2000.
- Jochen Rudolph. *Volatile Organic Compounds in the Atmosphere*, chapter Gas Chromatography-Isotope Ratio Mass Spectrometry, page 389 ff. Blackwell Publishing, Oxford, UK, 2007.
- Karri Saarnio, Minna Aurela, Hilkka Timonen, Sanna Saarikoski, Kimmo Teinilä, Timo Mäkelä, Mikhail Sofiev, Jarkko Koskinen, Pasi P. Aalto, Markku Kulmala, Jaakko Kukkonen, and Risto Hillamo. Chemical composition of fine particles in fresh smoke plumes from boreal wild-land fires in Europe. *Science of The Total Environment*, 408(12):2527 – 2542, 2010. ISSN 0048-9697.
- X. F. Sang, I. Gensch, B. Kammer, A. Khan, E. Kleist, W. Laumer, P. Schlag, S. H. Schmitt, J. Wildt, R. Zhao, E. L. Mungall, J. P. D. Abbatt, and A. Kiendler-Scharr. Chemical stability of levoglucosan: An isotopic perspective. *Geophysical Research Letters*, 43(10):5419–5424, 2016.
- Xue F. Sang, Iulia Gensch, Werner Laumer, Beatrix Kammer, Chuen Y. Chan, Guenter Engling, Andreas Wahner, Holger Wissel, and Astrid Kiendler-Scharr. Stable carbon isotope ratio analysis of anhydrosugars in biomass burning aerosol particles from source samples. *Environmental Science and Technology*, 46:3312–3318, 2012.
- James J. Schauer, Michael J. Kleeman, Glen R. Cass, and Bernd R. T. Simoneit. Measurement of Emissions from Air Pollution Sources. 3. $c_1 - c_{29}$ Organic Compounds from Fireplace Combustion of Wood. *Environmental Science & Technology*, 35:1716–1728, 2001.

Bibliography

- P. Seibert and A. Frank. Source-receptor matrix calculation with a Lagrangian particle dispersion model in backward mode. *Atmospheric Chemistry and Physics*, 4(1):51–63, 2004.
- Olaf Stein and Jochen Rudolph. Modeling and interpretation of stable carbon isotope ratios of ethane in global chemical transport models. *Journal of Geophysical Research: Atmospheres*, 112(D14), 2007.
- A. Stohl, M. Hittenberger, and G. Wotawa. Validation of the Lagrangian particle dispersion model flexpart against large-scale tracer experiment data. *Atmospheric Environment*, 32(24): 4245 – 4264, 1998. ISSN 1352-2310.
- A. Stohl, H. Sodemann, S. Eckhard, A. Frank, P. Seibert, and G. Wotawa. The Lagrangian particle dispersion model FLEXPART version 8.2, 2010.
- Andreas Stohl, Sabine Eckhardt, Caroline Forster, Paul James, Nicole Spichtinger, and Petra Seibert. A replacement for simple back trajectory calculations in the interpretation of atmospheric trace substance measurements. *Atmospheric Environment*, 36:4635–4648, 10 2002.
- Andreas Stohl, C Forster, S Eckhardt, Heidi Huntrieser, J Heland, H Schlager, H Aufmhoff, F Arnold, and O Cooper. A backward modeling study of intercontinental pollution transport using aircraft measurements. *Journal of Geophysical Research*, 2003.
- R. Stull. *An Introduction to Boundary Layer Meteorology*. Atmospheric and Oceanographic Sciences Library, Springer Netherlands, 2001.
- G. Zazzeri, D. Lowry, R.E. Fisher, J.L. France, M. Lanoisellé, and E.G. Nisbet. Plume mapping and isotopic characterisation of anthropogenic methane sources. *Atmospheric Environment*, 110:151 – 162, 2015. ISSN 1352-2310.
- B. Zhang. *Characterization of transport and transformation of air pollutants observed in the free troposphere over the Central North Atlantic*. PhD thesis, Michigan Technological University, 2015.
- B. Zhang, R. C. Owen, J. A. Perlinger, A. Kumar, S. Wu, M. Val Martin, L. Kramer, D. Helmig, and R. E. Honrath. A semi-Lagrangian view of ozone production tendency in North American outflow in the summers of 2009 and 2010. *Atmospheric Chemistry and Physics*, 14(5):2267–2287, 2014.
- Mei Zheng, Glen R. Cass, James J. Schauer, and Eric S. Edgerton. Source apportionment of PM_{2.5} in the Southeastern United States using solvent-extractable organic compounds as tracers. *Environmental Science & Technology*, 2002.

Erklärung

Hiermit versichere ich an Eides statt, dass ich die vorliegende Arbeit selbstständig und ohne die Benutzung anderer als der angegebenen Hilfsmittel angefertigt habe. Alle Stellen, die wörtlich oder sinngemäß aus veröffentlichten und nicht veröffentlichten Schriften entnommen wurden, sind als solche kenntlich gemacht. Die Arbeit ist in gleicher oder ähnlicher Form oder auszugsweise im Rahmen einer anderen Prüfung noch nicht vorgelegt worden. Ich versichere, dass die eingereichte elektronische Fassung der eingereichten Druckfassung vollständig entspricht.

Datum

Unterschrift